Chemical Geology 427 (2016) 17–34

Contents lists available at ScienceDirect

Chemical Geology

journal homepage: www.elsevier.com/locate/chemgeo

Deep weathering along a granite ridgeline in a subtropical climate

Wenjing Liu [a,b,c,*], Congqiang Liu [a,e], Susan L. Brantley [b], Zhifang Xu [a,c], Tong Zhao [a,c], Taoze Liu [e], Chong Yu [a,c], Dingshuai Xue [d], Zhiqi Zhao [e], Lifeng Cui [e], Zhuojun Zhang [c,e], Bailin Fan [e], Xin Gu [b]

[a] Key Laboratory of Shale Gas and Geoengineering, Institute of Geology and Geophysics, Chinese Academy of Sciences, Beijing 100029, China
[b] Earth and Environmental Systems Institute and the Department of Geosciences, The Pennsylvania State University, University Park, PA 16802, USA
[c] University of Chinese Academy of Sciences, Beijing 100049, China
[d] Key Laboratory of Mineral Resources, Institute of Geology and Geophysics, Chinese Academy of Sciences, Beijing 100029, China
[e] State Key Laboratory of Environmental Geochemistry, Institute of Geochemistry, Chinese Academy of Sciences, Guiyang, Guizhou 550002, China

ARTICLE INFO

Article history:
Received 8 May 2015
Received in revised form 30 January 2016
Accepted 13 February 2016
Available online 16 February 2016

Keywords:
Granite
Weathering
Pedogenesis
Soil formation
Interflow

ABSTRACT

Bulk chemical composition and mineralogy were examined in three soil profiles and a deeper 11-meter profile weathering on a granite ridgeline under subtropical climate conditions in south China. The weathering sequence is delineated by mineralogy and major element variations. Apatite, biotite, hornblende and plagioclase dissolve early during weathering, resulting in nearly 100% Ca and Na loss and significant Mg, Fe and P depletion at depth. The K-feldspar reaction front begins at the depth of depletion of plagioclase, leading to a loss of ~80% of the K at the land surface near the bottom of the ridgeline and almost 100% at the top. Dissolution of quartz and other silicates releases about 60% of Si in the profiles. Kaolinite is the dominant clay mineral and it transforms to gibbsite in the uppermost layer. The soil horizon (upper 100 cm) is the zone dominated by pedogenic processes, including active biological activity, physical erosion and influx of high concentrations of atmospheric components (especially CO_2 and O_2). The pedogenic processes are characterized by low pH (~4.54 to 5.85), high clay content (kaolinite: 6–16 wt.%; gibbsite: 2–8 wt.%) and total organic carbon content (0.13–3.93%) and intensive fracturing and dissolution of quartz and K-feldspar compared with the lower horizons.

Accumulation of organic material and resistant minerals downslope is attributed to down-ridge movement of water (termed here, interflow) and weathering products in the uppermost 100 cm down the ridgeline. Using a mass balance model calculation for the catena that assumes steady-state soil thickness at all sites, the bottom profile shows the highest apparent total chemical weathering loss rate (~14 g m^{-2} y^{-1}) whereas the middle position shows the highest physical erosion loss rate (~44 g m^{-2} y^{-1}). SiO_2 accounts for about 84% of the chemical weathering outflux from the soil horizons along the ridgeline hillslope. Chemical weathering rates at the bottom of the hillslope may be accelerated by high concentrations of organic material and by dissolution of kaolinite.

This study demonstrates that mineral reaction fronts in granite become separated over depth intervals of meters and that elemental fluxes and release mechanisms vary with position along a ridgeline catena.

1. Introduction

Weathering is the major process of mass transfer from continent to the ocean (Bouchez and Gaillardet, 2014), and also is a key process controlling the global cycling of carbon, and the nutrient supply to ecosystems. Continental weathering, silicate chemical weathering in particular, converts atmospheric CO_2 into alkalinity and on a global scale influences ocean chemistry and imposes a net drawdown of atmospheric CO_2 that modulates global climate (Walker James et al., 1981; Berner et al., 1983; Volk, 1987; Dupré et al., 2003). Long term climatic evolution is driven by the balance between solid earth degassing and continental silicate weathering (Goddéris et al., 2008).

Catchment and soil profile studies are two types of studies that address questions related to silicate weathering by studying systems in 3-dimensions or 1-dimension respectively. For example, the geochemistry of riverine dissolved loads has been widely used to quantify material fluxes including C on regional and global scales (Gaillardet et al., 1999; Dessert et al., 2003; Bouchez and Gaillardet, 2014 and reference there). However, rivers are natural integrators of the weathering and erosion processes in their drainage areas; multiple factors are synthesized in river loads. To understand the details of weathering, it is necessary to explore weathering in pedogenic profiles in the river basins. Profiles of regolith can provide a long-term record of the Earth's Critical Zone (Brantley and Lebedeva, 2011). Researchers explore the weathering mechanisms, material transport, and controlling environment factors for silicate weathering process. Pioneering weathering studies at the profile scale have recently focused on basalt (Prudêncio et al., 1993; Rye and Holland, 2000; Ma et al., 2007; Ma et al., 2010a; Babechuk et al., 2014),

* Corresponding author.
E-mail address: liuwenjing@mail.iggcas.ac.cn (W. Liu).

http://dx.doi.org/10.1016/j.chemgeo.2016.02.014
0009-2541/

shale (Manikyamba et al., 2008; Tuttle and Breit, 2009; Jin et al., 2010; Ma et al., 2010b; Jin and Brantley, 2011; Ma et al., 2011) and granite (see the references in the following paragraph). Mineralogical, geochemical and geophysical methods have been integrated for the regolith evolution study (Braun et al., 2009).

Granitic rocks are important subjects for the study of continental weathering since the Earth's upper continental crust is known to be, on average, of granodioritic composition (Taylor and McLennan, 1985; McLennan, 2001; Hurowitz et al., 2006). In fact, granitic rocks constitute ~25% of the land surface of the upper crust (Oliva et al., 2003). Numerous elements and isotopic indices have been proposed to characterize and quantify chemical weathering processes of granite (Law et al., 1991; Mongelli, 1993; Blum and Erel, 1997; Minařík et al., 1998; Land and Ohlander, 2000; White et al., 2001; Jeong and Bin Kim, 2003; Kirschbaum et al., 2005; Négrel, 2006; Ceryan et al., 2008; Duzgoren-Aydin and Aydin, 2009; Pett-Ridge et al., 2009; Shalkowski et al., 2009). Previous studies on granite weathering environments emphasize that the dependence between temperature and runoff, and chemical weathering is complicated by the presence/depth of soil cover (Oliva et al., 2003). The effects of weathering on major and trace element distributions through profiles are extensively studied in previous documents in order to elucidate weathering and erosion processes (Nesbitt, 1979; Middelburg et al., 1988; Burkins et al., 1999; Turner et al., 2003; Kamei et al., 2012). Most studies have been conducted by assessing a pedogenic profile for its geochemical variations (so-called “one dimensional weathering” (Jin et al., 2010)). Only a few studies have focused on the distribution of pedogenic profiles on granite in two-dimensions (catena) or in three dimensions (a catchment). Notable studies of granite weathering across hillslope scale include quantification of chemical weathering rates for soil-mantled hillslopes in New South Wales, Australia (Green et al., 2006; Yoo et al., 2007) and chemical transferring along catenas in southern Africa (Bern et al., 2011; Khomo et al., 2013).

Understanding the solute fluxes out of granitic systems, as recorded in the profiles across a landscape, is a key problem in Earth's Critical Zone evolution research. This study is designed to investigate the evolution of a granite ridgeline hill slope located in subtropical climate by examining bulk chemical composition, mineralogy and weathering characteristics of a series of weathering profiles distributed along a sloping ridgeline located in south China. This catena is a transect along the roughly sloping ridgeline. The warm and humid climate and gently hilly landforms in the study area are favorable for chemical weathering, making it an ideal site for granite weathering process research. Detailed discussions of coupled mineral and element variation and their implication on weathering reaction fronts during granite process are presented. Lateral transport flux of materials, weathering and erosion rate along the hillslope are calculated for the soil horizon of the catena and are furthermore explored for granite weathering impacting factors.

2. Materials and methodology

2.1. Geology and climate background of study area

The studied hill is in Longnan, Jiangxi province, south China. Jiangxi province is located predominantly in the region of lower montane wet forests, with moderate relief and an average elevation of 300–400 m. The mean annual temperature is 11.6–19.6 °C and the mean annual precipitation is around 1600 mm. The rainfall is distributed unevenly through the year, with more than 50% of the precipitation during April to July. The studied region has well-developed vegetation in a subtropical moist rainy climate.

The profiles are located on a hill on the Yanshanian granite complex. The hill is part of a granitoid complex in East Nanling Region, with an outcrop area of more than 400 km^2. The granitoid complex is reported as an A type granite, composed of a K-feldspar granite and accompanying syenite (Fan and Chen, 2000). The Rb–Sr isochron age of this K-feldspar granite is 178.2 ± 0.84 Ma (Fan and Chen, 2000). The bedrock granite is medium to coarse grained and dominated by phenocrysts of quartz, K-feldspar and plagioclase and by smaller amounts of biotite, hornblende and chlorite as observed in hand specimen of bedrock. Sinian–Cambrian sandstone and mudstone, the Devonian–Triassic clastic and carbonate rock, and the Indo-China epoch granite are located to the east, south and west of the granitoid complex respectively. Late Cretaceous red bed sediments cover part of the complex in the north (Fan and Chen, 2000; Chen et al., 2004; Li et al., 2007).

2.2. Field observations and sampling

The deepest study profile (JLN-S1) is located near the bottom of a hill (elevation of land surface = 210 m) and is exposed in a road cut (Fig. 1). Three additional soil profiles (JLN-S2, S3, S4) were sampled along the ridgeline hill slope above the outcrop, and all are developed on the Yanshanian granite complex. The uppermost elevation of the first-order channel that hosts a perennial stream in this very small catchment is 246 m; the outlet of the stream is at the road close to JLN-S1. The stream is incising bedrock along the entire channel. A spring was observed at 214 m elevation, between JLN-S1 and the stream. In addition to the outcrop samples and soil samples, bedrock samples that appeared fresh and unweathered were sampled (Fig. 1). Specifically, four bedrock samples were collected close to the bottom of the weathering profile JLN-S1 in the streambed.

The road-cut profile JLN-S1, exposed at the bottom of the hill, is an 1100 cm deep in-situ granite weathering profile, with upwardly increasing alteration extent. We follow the definitions of layers used by Pavich et al. (1989): bedrock (unaltered protolith); weathered rock (firm, brittle, altered rock material that is difficult to excavate); saprolite (weak, easily excavated with a shovel material that has the texture and structure of the bedrock); massive subsoil (soil-like material that does not demonstrate layering or structure of bedrock); and soil (layered material that does not show bedrock structure). The lower boundary of soil in this profile (i.e. the depth where a transition occurs from layered soil-like material to massive, unlayered, largely immobile and in-place material that does not retain evidence of the original structure of the rock) can be observed at a depth of about 100 cm in the field. The section above 100 cm of JLN-S1 is characterized by a loose texture, higher amount of sticky clay mineral, and brown to red coloration. There is a quartz vein at the depth of 170–190 cm, and a vein dominated by plagioclase at a depth of around 700 cm.

The four bedrock samples collected close to the bottom of the JLN-S1 weathering profile in the streambed appeared to be good samples of parent material based on their mineral composition and texture. Bulk composition, mineralogy and low values of Loss on Ignition (LOI) are consistent with the inference that these samples provide a good estimate of parent rock composition (see in Section 3.3). Gradual alteration of the parent rock to saprolite upward and formation of soil at the top was easily observed in the field (see description in caption of Fig. 1).

Higher on the catena are JLN-S2 (located 24 m upslope from JLN-S1, at the elevation of 240 m) and JLN-S3 (36 m from JLN-S1, at the elevation of 250 m), both located at the middle of the hill along the ridge, and JLN-S4 that is located at the hill top (63 m from JLN-S1, at the elevation of 260 m). These three soil profiles were sampled to 120 cm deep (Fig. 1). The soil profiles share similar color and texture features with the upper part of JLN-S1. The four profiles were thus considered as a catena that demonstrated weathering along the ridgeline hillslope.

JLN-S1 was sampled from top to bottom over its entire 1100 cm span by digging inward by about 100 cm into the original exposed vertical surface. The depth interval for each sample was decided in the field based on texture and color changes in the profile (see Table 1). The deepest incipient weathering (interface between bedrock and weathered rock) layer was defined to occur above the layer that showed

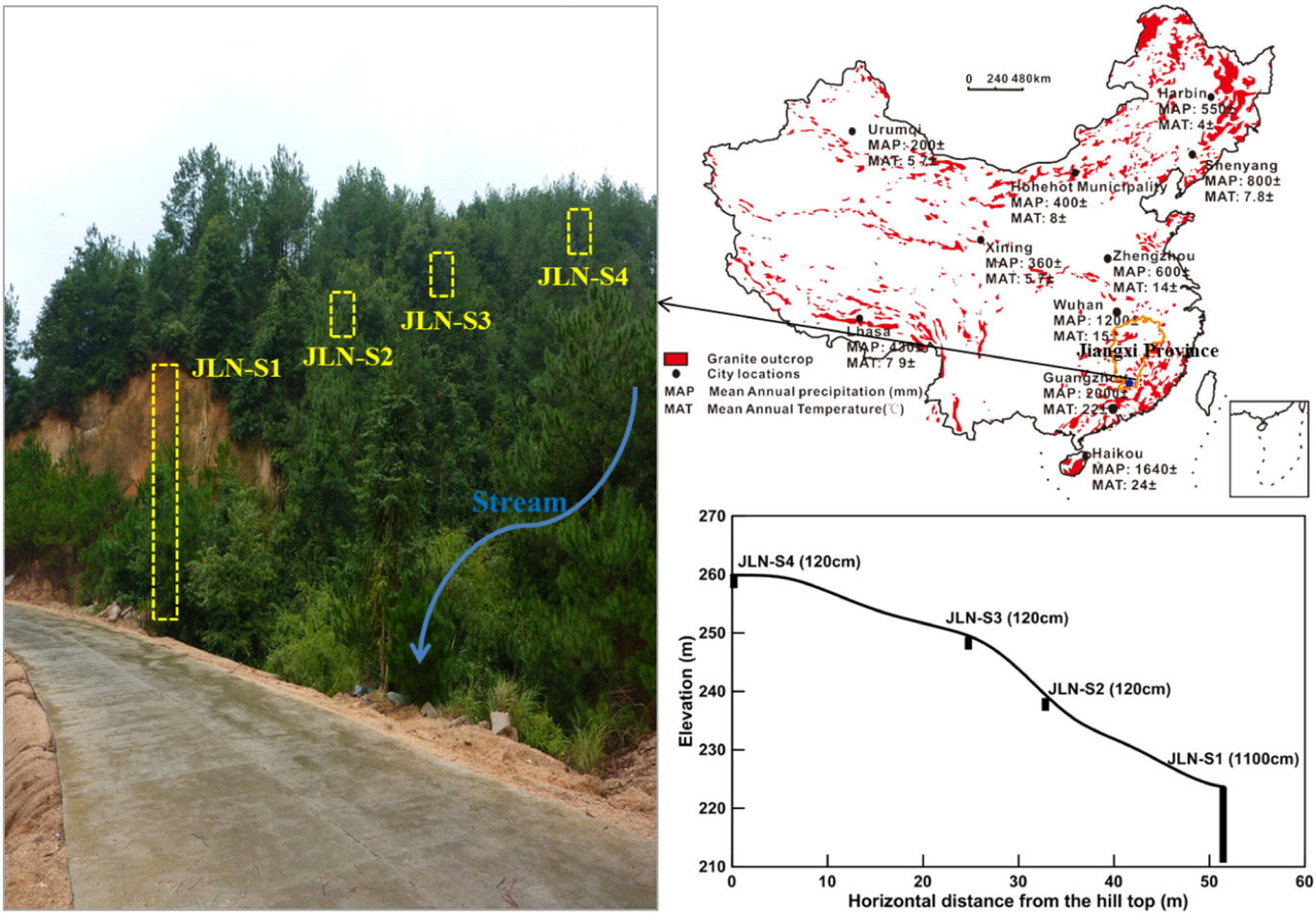

Fig. 1. A photograph, site location map, and cross section of the profiles. Field observations for profile JLN-S1 include the following: below 400 cm depth, the weathering material is white-gray colored, with a texture indicative of primary mineral weathering, as well as coarse, angular quartz fragments and grains; from 400 to ~200 cm, the profile consists of yellow and brown massive soil with smaller quartz fragments and with almost total disappearance of feldspar; above 200 cm, the massive soil color changes from brown to red-brown, and the texture becomes stickier upwards; above 100 cm, the color turns darker brown and the texture turns stickier. In this uppermost layer, quartz fragments are smaller and appear to be broken.

i) little apparent mineralogical change as observed visually, and ii) was observed to be very hard with respect to peening by a hammer.

Three soil profiles (JLN-S2, S3, S4, 120 cm deep) show generally the same color and texture as the upper 120 cm of JLN-S1 observing visually. For each of the profile, a pit was dug and then the soil samples were collected from the bottom upward to the surface of the profile. Each sample represents a 5 centimeter depth interval. About 1.5 kg of material was taken for each sample.

2.3. Analytical procedures

2.3.1. Basic physical and chemical analyses

Samples for soil density measurement were collected with 100 mL cutting rings. The samples in the rings were transferred into pre-weighed beakers and dried at 105 °C in the laboratory. Bulk density was calculated from the volume and mass of each dried sample. Several pieces of dry rock for each bedrock sample were weighed and their volumes were measured by water displacement. Then each rock piece density was determined and they were averaged to get the sample density.

Values of pH were determined on 1:2.5 soil:CO_2-free pure water mixtures with a Sension 156 multiple-parameters analyzer from HACH. Soil cation exchange capacity (CEC) was determined as all the exchangeable cations (e.g., K^+, Na^+, Ca^{2+}, Mg^{2+}, NH_4^+, H^+, Al^{3+}) contained in the soil (cmol(+)/kg), at a given pH value (=7) (potential CEC). Here, cmol(+) means 10^{-2} mole positive charge.

CEC indicates the cation contents occupied by the clay mineral interlayers. It was analyzed by the Ammonium Acetate (NH_4OAC) Method at pH 7.0 (Modified from Pansu and Gautheyrou, 2007): the sample was first NH_4^+-saturated by mixing it with 1 M NH_4OAC (pH 7.0). The supernatant was collected and analyzed for dissolved species by Inductively Coupled Plasma Optical Emission Spectrometry (ICP-OES) ($M_{leachate}$ in cmol(+)/kg soil, represents the cation content leached by NH_4OAC from each kg soil). The residue was processed to calculate CEC. The residual soil was treated with 95% alcohol to remove excess NH_4OAC and then rinsed into a Kjeldahl flask. Then, solid MgO was added and the mixture was distilled. Finally, the distilled NH_4^+ from the Kjeldahl flask was absorbed by boric acid solution, and titrated with HCL. CEC was calculated as the amount of NH_4^+ that each sample released.

The soil base saturation (BS) was calculated as the amount of soil exchangeable non-acid-causing base ions expressed as a percentage of the soil cation exchange capacity (Bloom and Skyllberg, 2011):

$$BS = \left(K^+_{leachate} + Na^+_{leachate} + Ca^{2+}_{leachate} + Mg^{2+}_{leachate}\right)/CEC * 100\%. \quad (1)$$

$K^+_{leachate}$, $Na^+_{leachate}$, $Ca^{2+}_{leachate}$, and $Mg^{2+}_{leachate}$ are the concentrations (in cmol(+)/kg soil) of the supernatant collected in the CEC procedure.

Grain size analysis was conducted by laser method on a Malvern 2000.

2.3.2. Mineral composition analysis

Mineralogical analysis was completed using X-ray diffraction (XRD, D/Max-2400). The instrument parameters were: CuK, 40 kV, 60 mA,

Table 1
pH value, density and grain size composition of JLN-S1 weathering profile.

Sample no.	Depth (cm)	Density g/cm^3	pH value	Grain size composition (%)		
				20–2000 μm	2–20 μm	<2 μm
JLN-S1-01	0–20	0.88	4.65			
JLN-S1-02	20–30	1.25	4.75			
JLN-S1-03	30–40	1.30	4.91	30.5	40.65	28.85
JLN-S1-04	40–50	1.40	4.91	28.44	39.53	32.03
JLN-S1-05	50–60	1.27	4.98	38.74	32.51	28.75
JLN-S1-06	60–70	1.38	5.06	36.8	30.59	32.6
JLN-S1-07	70–80	1.41	5.18	33.48	41.94	24.59
JLN-S1-08	80–90	1.40	5.2	31.39	41.34	27.27
JLN-S1-09	90–100	1.50	5.27	50.54	31.99	17.47
JLN-S1-10	100–110	1.41	5.34	42.83	35.33	21.84
JLN-S1-11	110–120	1.34	5.27	55.72	27.86	16.42
JLN-S1-12	120–130	1.37	5.32	53.23	29.36	17.41
JLN-S1-13	130–140	1.36	5.34	56.19	28.11	15.7
JLN-S1-14	140–150	1.39	5.36	49.81	32.06	18.13
JLN-S1-15	150–160	1.38	5.42	55.11	29.6	15.29
JLN-S1-16	160–170	1.27	5.48	46.52	35.32	18.16
JLN-S1-17	170–180	1.35	5.6			
JLN-S1-18	180–190	1.49	5.49			
JLN-S1-19	190–200	1.36	5.76	60.55	25.37	14.07
JLN-S1-20	200–220		5.72	53.28	30.46	16.25
JLN-S1-21	220–240		5.76	67.71	21.52	10.77
JLN-S1-22	240–260		5.7	61.34	26.01	12.65
JLN-S1-23	260–280		5.71	62.84	25.6	11.56
JLN-S1-24	280–300		5.76	58.21	29.37	12.41
JLN-S1-25	300–320		6.16	67.27	23.36	9.37
JLN-S1-26	320–340		6.24	64.05	26.24	9.71
JLN-S1-27	340–360		6.2	72.18	20.7	7.12
JLN-S1-28	360–380		5.88	86.06	10.89	3.05
JLN-S1-29	380–400		6.05	93.2	6.8	0
JLN-S1-30	400–420		6.18	90.39	8.11	1.5
JLN-S1-31	420–440		6.07	88.13	9.95	1.92
JLN-S1-32	440–460		6.26	95.06	4.94	0
JLN-S1-33	460–480		6.3	95.17	4.83	0
JLN-S1-34	480–500		6.23	94.76	5.24	0
JLN-S1-35	500–520		6.17	91.78	8.22	0
JLN-S1-36	520–560		6.23	92.64	7.36	0
JLN-S1-37	560–580		6.2	92.84	7.16	0
JLN-S1-38	580–600		6.29	88.8	9.41	1.8
JLN-S1-39	600–620		6.4	83.1	13.85	3.06
JLN-S1-40	620–640		6.38	86.56	11.51	1.93
JLN-S1-41	640–660		6.09	88.79	9.22	1.99
JLN-S1-42	660–680		6.2	75.21	20.64	4.15
JLN-S1-43	680–700		6.5	87.63	10.57	1.8
JLN-S1-44	700–720		6.31	91.85	8.15	0
JLN-S1-45	720–740		6.38	85.96	11.76	2.28
JLN-S1-46	740–760		6.4	89.48	8.82	1.7
JLN-S1-47	760–780		6.43	85.24	12.22	2.54
JLN-S1-48	780–800		6.34	88.45	9.64	1.91
JLN-S1-49	800–850		6.49	80.66	15.85	3.49
JLN-S1-50	850–900		6.49	81.89	14.74	3.37
JLN-S1-51	900–950		6.64	82.53	14.23	3.24
JLN-S1-52	950–1000		6.59	94	6	0
JLN-S1-53	1000–1100		6.68	93.63	6.37	0

scanning area: 2Q = 2–60, and scanning method: 8°/min. The mineral weight contents were calculated by Rietveld refinement of powder X-ray diffraction patterns.

2.3.3. Major composition analysis

The major element bulk composition was analyzed using X-ray fluorescence (Axios XRF): results were expressed as, SiO_2, TiO_2, Al_2O_3, MnO, MgO, CaO, Na_2O, K_2O, P_2O_5, FeO_T (including Fe(II) and Fe(III)). Chinese national standard samples GBW07101-07114 and GBW07295-07429 were used to monitor the data quality. The best analysis range and accuracy for each major composition are given in Appendix A. LOI (Loss on Ignition) data were calculated from the mass reduction of 1 g soil combusted at 950 °C by 1 h. All the major element contents listed above were measured within the optimal analysis range for the Axios XRF, with the exception of the upper profile samples which had slightly lower values of Na, Ca, Mg, and Mn contents. These elements were therefore measured by acid-digestion and determination using ICP-OES. The Zr content of the bedrock samples was also measured from the same digestion solution using Inductively Coupled Plasma Mass Spectrometry (ICP-MS).

In this study, the percentage increase or decrease of any element X content in a profile sample, relative to fresh parent rock was expressed as PERC. CHANGE (Nesbitt, 1979) as defined below:

$$\text{PERC.CHANGE} = \left[(X/Ti)_{\text{sample}}/(X/Ti)_{\text{parent}} - 1\right] * 100 \quad (2)$$

where X and Ti are the concentrations of a mobile element and the inert element Ti respectively; sample and parent indicate the profile samples and bedrock samples respectively. PERC. CHANGE is equivalent to the weathering index τ notation (Brimhall and Dietrich, 1987) when expressed in percentage. In addition, the CIA (chemical index of alteration) was used to denote the weathering extent of the profile samples. It was first used by Nesbitt and Young (1982) to evaluate weathering intensity in sedimentary rocks:

$$\text{CIA} = Al_2O_3/(Al_2O_3 + CaO^* + Na_2O + K_2O) * 100. \quad (3)$$

In this equation, all constituent concentration data are expressed in moles/kg. CaO^* equals the CaO content in the silicate fraction of the sample. In the granite rock, Ca was dominantly in plagioclase, and only present to a minor extent as calcite, apatite and other Ca-containing minerals (see later discussion). Meanwhile, all the saprolite and rock samples have moles Ca/moles Na < 1, again consistent with the overall lack of carbonate. Thus no correction was needed for carbonate in calculating the CIA values (Rudnick et al., 2004). In this study, we calculate CaO^* of the profile samples by the formula: $Ca_{silicate} = Ca_{bulk} - Ca_{leachate}$. Here, $Ca_{silicate}$, Ca_{bulk} and $Ca_{leachate}$ refer to the Ca content (moles/kg) in the silicate fraction of the profile or rock sample, in the bulk sample and in the supernatant from the CEC procedure respectively.

Dried bulk soil samples were treated with 0.5 mol/L HCl solution for 24 h to remove the inorganic carbon, and then total organic carbon (TOC) contents were measured with a PE2400-II element analyzer.

3. Results

3.1. Physical and chemical characteristics of the soil and weathering profiles

Grain size variation of JLN-S1 is shown in a depth profile in Fig. 2, as well as pH, CEC and BS. These major chemical characteristics (pH, CEC, BS) and soil density for the bulk samples are reported in Tables 1, 2 and 3. Rock density was calculated (2.6 ± 0.3 g/cm^2) by averaging the density for bedrock samples.

The pH values range between 4.54 and 6.68, and generally decrease upward in all profiles, while CEC values increase upward within a range of 4.23 to 14.55 (cmol(+)/kg soil). In the roadcut profile JLN-S1, the trends for these analyses as well as grain size vary much more sharply above 400 cm than below. The three grain-size fractions (<2 μm, 2–20 μm and 20–2000 μm) are roughly constant deeper than 400 cm at around 0%, 8% and 90% respectively. Above 400 cm, both percentages of <2 μm and 2–20 μm fractions increase to about 30–40% at the surface of the profile while the 20–2000 μm fraction decrease to about 30% at the top. No other rock fragments larger then 2 mm were observed except for some occasional quartz rock fragments.

Some patterns can be seen among the different profiles (Fig. 2). For example, JLN-S4 (hilltop) shows the lowest pH and BS values compared to the other profiles. The BS trends differ from profile to profile. BS ranges from 12.40 to 65.96% in JLN-S1 (foot of the hill), decreasing upward in the profile above 400 cm, while the BS values of JLN-S4 profile at the top of the hill are in the range of 1.57–27.83%, increasing upward. The two middle profiles JLN-S2 and -S3 show BS values in the middle of the range between the hilltop and foot profiles.

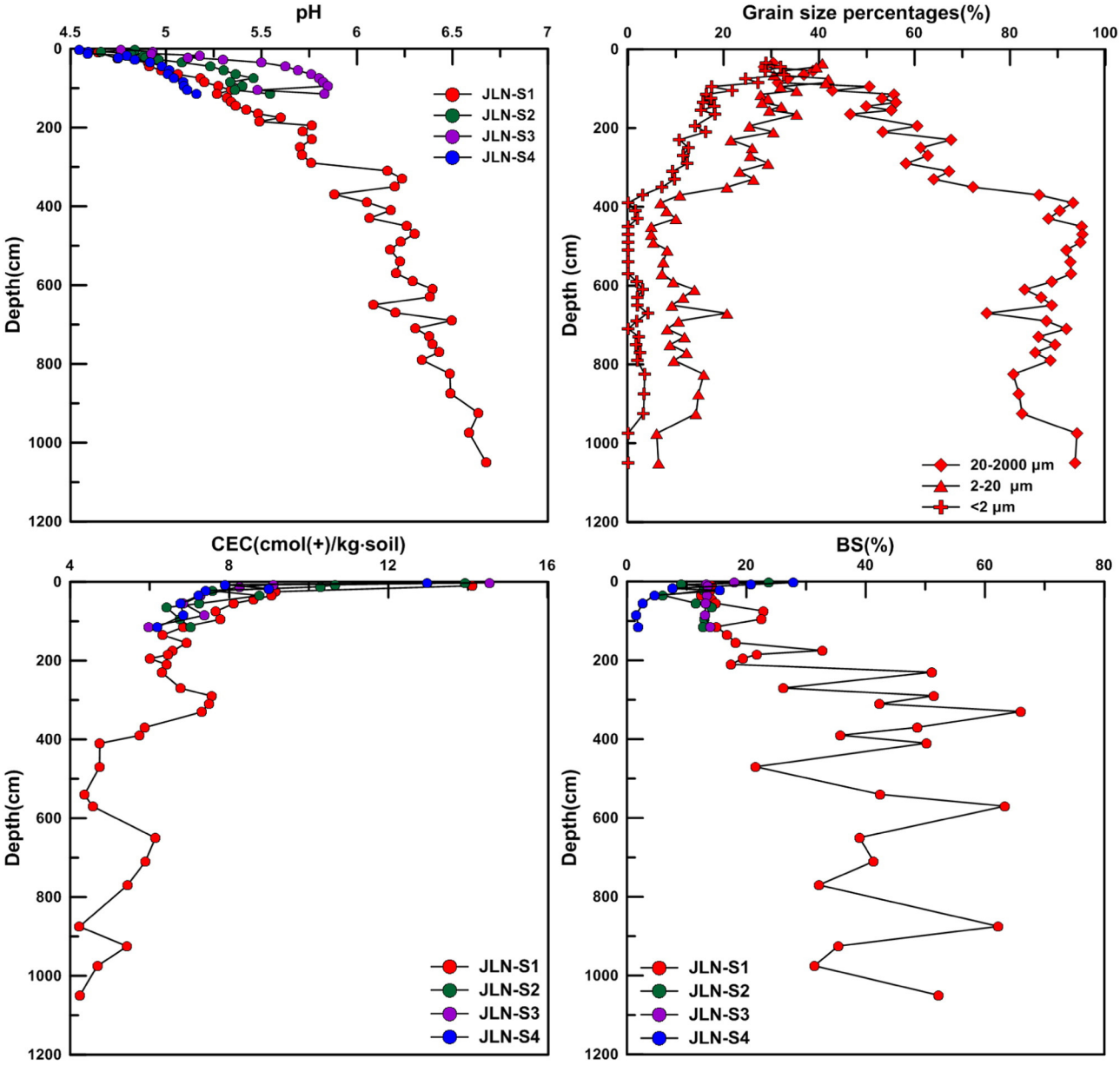

Fig. 2. Variations in pH, cation exchange capacity (CEC), base saturation (BS) and grain size composition versus depth (JLN-S1) for the studied profiles as shown in the legend.

Table 2
pH value and density of JLN-S2, JLN-S3, and JLN-S4 soil profiles.

Depth (cm)	Sample no.	pH value	Density g/cm^3	Sample no.	pH value	Density g/cm^3	Sample no.	pH value	Density g/cm^3
0–5	JLN-S2-01		0.75			0.95	JLN-S4-01	4.54	1.15
5–10	JLN-S2-02	4.66	1.29	JLN-S3-02	4.93	1.22	JLN-S4-02	4.59	1.28
10–15	JLN-S2-03	4.82	1.29	JLN-S3-03	4.92	1.39	JLN-S4-03	4.59	1.21
15–20	JLN-S2-04	4.88	1.27	JLN-S3-04	5.18	1.39	JLN-S4-04	4.79	1.31
20–25	JLN-S2-05	4.89	1.30	JLN-S3-05	5.11	1.17	JLN-S4-05	4.75	1.25
25–30	JLN-S2-06	4.96	1.32	JLN-S3-06	5.3	1.24	JLN-S4-06	4.84	1.28
30–40	JLN-S2-07	5.08	1.33	JLN-S3-07	5.5	1.16	JLN-S4-07	4.92	1.20
40–50	JLN-S2-08	5.23	1.40	JLN-S3-08	5.62	1.30	JLN-S4-08	4.98	1.26
50–60	JLN-S2-09	5.3	1.44	JLN-S3-09	5.69	1.24	JLN-S4-09	5.02	1.20
60–70	JLN-S2-10	5.36	1.33	JLN-S3-10	5.76	1.25	JLN-S4-10	5.01	1.26
70–80	JLN-S2-11	5.46	1.34	JLN-S3-11	5.8	1.23	JLN-S4-11	5.04	1.24
80–90	JLN-S2-12	5.34	1.28	JLN-S3-12	5.82	1.26	JLN-S4-12	5.09	1.34
90–100	JLN-S2-13	5.4	1.33	JLN-S3-13	5.85	1.20	JLN-S4-13	5.09	1.32
100–110	JLN-S2-14	5.36	1.25	JLN-S3-14	5.48	1.09	JLN-S4-14	5.11	1.31
110–120	JLN-S2-15	5.55	1.36	JLN-S3-15	5.83	1.15	JLN-S4-15	5.16	1.23

Table 3
CEC, BS, CIA value and bulk composition of profiles.

Sample no.	Depth (cm)	CEC (cmol(+)/kg)	Exchangeable base (cmol(+)/kg)	BS (%)	CIA	SiO_2 (%)	Al_2O_3 (%)	K_2O (%)	Na_2O (%)	CaO (%)	MgO (%)	FeO_T (%)	MnO (%)	TiO_2 (%)	P_2O_5 (%)	LOI (%)
JLN-S1-01	0–20	14.12	1.36	14.16	88.01	62.02	17.90	2.06	0.07	0.04	0.13	4.17	0.02	0.37	0.04	13.81
JLN-S1-02	20–30	9.16	0.92	13.87	91.44	66.96	18.09	1.45	0.04	0.02	0.11	4.28	0.01	0.33	0.03	9.30
JLN-S1-03	30–40	9.06	0.85	12.40	91.98	55.57	25.47	1.92	0.05	0.02	0.17	5.82	0.01	0.43	0.03	11.42
JLN-S1-04	40–50	8.61	0.89	14.23	92.44	64.00	20.86	1.47	0.04	0.02	0.14	4.85	0.01	0.35	0.03	9.15
JLN-S1-05	50–60	8.11	0.89	14.90	92.25	67.64	18.47	1.33	0.04	0.02	0.13	4.30	0.01	0.31	0.02	8.01
JLN-S1-07	70–80	7.66	1.17	22.91	92.42	74.71	14.50	1.00	0.03	0.02	0.10	3.44	0.01	0.24	0.02	5.97
JLN-S1-09	90–100	7.78	1.16	22.49	91.84	77.54	13.30	1.00	0.03	0.02	0.09	3.05	0.01	0.22	0.02	5.42
JLN-S1-11	110–120	6.84	0.78	14.96	90.72	75.10	14.72	1.30	0.04	0.01	0.09	3.21	0.02	0.24	0.02	5.76
JLN-S1-13	130–140	6.33	0.75	16.78	90.15	75.86	14.14	1.33	0.04	0.01	0.08	3.00	0.01	0.23	0.01	5.59
JLN-S1-15	150–160	6.92	0.80	18.18	88.61	67.95	17.98	2.00	0.06	0.02	0.11	3.91	0.02	0.31	0.02	7.28
JLN-S1-17	170–180	6.58	1.28	32.76	89.09	88.36	6.22	0.63	0.02	0.02	0.04	1.51	0.01	0.11	0.01	2.56
JLN-S1-18	180–190	6.46	0.89	21.75	88.67	85.66	7.80	0.84	0.03	0.01	0.06	1.98	0.01	0.15	0.01	3.12
JLN-S1-19	190–200	6.01	0.75	19.42	86.62	78.76	12.26	1.64	0.04	0.02	0.08	2.75	0.02	0.21	0.02	4.63
JLN-S1-20	200–220	6.43	0.73	17.42	86.99	74.60	14.40	1.87	0.05	0.02	0.09	3.24	0.02	0.25	0.02	5.46
JLN-S1-21	220–240	6.30	1.80	51.07	84.99	83.68	9.28	1.41	0.04	0.02	0.06	2.12	0.02	0.16	0.01	3.48
JLN-S1-23	260–280	6.77	1.06	26.22	83.71	73.64	14.95	2.55	0.06	0.02	0.08	3.17	0.07	0.24	0.02	5.28
JLN-S1-24	280–300	7.56	2.15	51.47	84.81	72.81	15.43	2.40	0.06	0.02	0.09	3.37	0.05	0.27	0.02	5.81
JLN-S1-25	300–320	7.49	1.77	42.30	83.49	70.60	16.77	2.85	0.07	0.04	0.10	3.37	0.07	0.27	0.02	6.26
JLN-S1-26	320–340	7.32	2.63	65.96	81.43	70.00	16.96	3.34	0.08	0.04	0.10	3.36	0.08	0.26	0.02	6.18
JLN-S1-28	360–380	5.87	1.71	48.66	74.56	68.69	17.65	5.35	0.11	0.02	0.07	2.94	0.04	0.29	0.02	5.20
JLN-S1-29	380–400	5.74	1.35	35.73	70.25	71.76	15.75	5.88	0.14	0.02	0.07	2.38	0.05	0.26	0.01	4.09
JLN-S1-30	400–420	4.75	1.48	50.17	72.13	68.34	17.19	5.90	0.12	0.02	0.08	3.04	0.06	0.30	0.02	4.78
JLN-S1-33	460–480	4.74	0.73	21.59	72.23	69.60	16.55	5.66	0.11	0.02	0.08	3.26	0.06	0.28	0.02	4.58
JLN-S1-36	520–560	4.36	1.23	42.40	68.94	71.65	15.32	6.13	0.13	0.02	0.06	2.07	0.04	0.21	0.01	3.60
JLN-S1-37	560–580	4.57	1.79	63.31	69.80	69.70	16.57	6.32	0.16	0.02	0.07	2.45	0.04	0.26	0.01	4.11
JLN-S1-41	640–660	6.14	1.67	38.93	66.58	71.41	14.61	6.19	0.34	0.03	0.07	2.58	0.13	0.21	0.02	3.38
JLN-S1-44	700–720	5.89	1.52	41.35	61.64	70.64	15.61	6.49	1.49	0.08	0.07	2.73	0.05	0.23	0.02	2.92
JLN-S1-47	760–780	5.44	1.15	32.19	67.30	71.88	15.51	5.84	0.65	0.05	0.08	2.52	0.08	0.26	0.02	3.48
JLN-S1-50	850–900	4.23	1.57	62.26	66.51	72.67	14.68	6.02	0.47	0.04	0.10	2.51	0.06	0.24	0.01	2.78
JLN-S1-51	900–950	5.43	1.14	35.39	65.17	72.93	14.25	5.84	0.70	0.05	0.10	2.47	0.06	0.23	0.01	3.06
JLN-S1-52	950–1000	4.68	0.97	31.42	59.35	72.77	14.70	6.17	1.90	0.10	0.08	2.25	0.07	0.21	0.02	2.52
JLN-S1-53	1000–1100	4.24	1.37	52.23	57.77	76.33	12.70	5.37	1.94	0.11	0.07	2.01	0.06	0.18	0.02	1.96
JLN-R1					49.76	74.10	12.89	5.24	3.10	0.87	0.18	2.43	0.06	0.20	0.03	0.60
JLN-R2					48.96	73.00	13.07	5.10	3.34	1.02	0.21	2.76	0.07	0.22	0.04	0.48
JLN-R3					49.99	73.58	13.25	5.15	3.19	0.95	0.18	2.37	0.07	0.20	0.04	0.42
JLN-R4					52.37	74.64	12.68	4.68	3.18	0.48	0.21	2.97	0.05	0.24	0.05	0.68
JLN-S2-01	0–5	13.93	1.94	23.71	93.27	66.97	16.05	0.85	0.03	0.07	0.10	3.71	0.02	0.28	0.03	12.55
JLN-S2-02	5–10	10.66	0.63	9.07	94.35	69.45	16.53	0.82	0.03	0.02	0.09	3.85	0.01	0.28	0.02	9.87
JLN-S2-03	10–15	10.29	0.87	13.54	95.31	63.36	20.19	0.80	0.03	0.03	0.11	4.65	0.02	0.31	0.03	11.39
JLN-S2-05	20–25	7.58	0.66	12.85	95.97	65.72	20.51	0.72	0.02	0.02	0.11	4.60	0.01	0.30	0.02	9.33
JLN-S2-07	30–40	8.76	0.42	6.02	95.86	68.04	19.33	0.69	0.02	0.02	0.10	4.27	0.01	0.30	0.02	8.39
JLN-S2-09	50–60	7.25	0.62	11.54	95.62	70.13	18.26	0.71	0.02	0.01	0.08	4.02	0.01	0.30	0.02	7.57
JLN-S2-10	60–70	6.42	0.65	14.21	95.12	76.28	14.57	0.62	0.02	0.02	0.08	3.22	0.01	0.23	0.02	5.85
JLN-S2-13	90–100	6.76	0.59	12.95	94.44	66.54	20.01	1.01	0.03	0.01	0.08	4.24	0.01	0.32	0.02	8.19
JLN-S2-15	110–120	7.03	0.62	12.77	94.07	76.60	14.23	0.76	0.03	0.01	0.06	3.10	0.01	0.23	0.02	5.82
JLN-S3-01	0–5	14.55	1.65	17.97	95.14	68.61	17.86	0.74	0.02	0.03	0.08	3.70	0.02	0.25	0.02	10.01
JLN-S3-02	5–10	9.11	0.82	13.31	95.06	65.40	20.41	0.90	0.03	0.01	0.08	4.33	0.02	0.30	0.02	9.53
JLN-S3-03	10–15	8.25	0.76	13.55	95.75	68.45	19.02	0.69	0.02	0.02	0.09	3.95	0.01	0.25	0.02	8.52
JLN-S3-5	20–25				96.07	66.47	20.50	0.70	0.02	0.02	0.08	4.17	0.01	0.28	0.02	8.77
JLN-S3-07	30–40	7.28	0.68	13.46	95.89	74.42	15.62	0.52	0.03	0.02	0.09	3.15	0.01	0.21	0.02	6.59
JLN-S3-09	50–60	6.85	0.64	13.23	96.12	69.16	18.91	0.65	0.02	0.01	0.07	3.81	0.01	0.27	0.02	7.79
JLN-S3-12	80–90	7.37	0.66	13.04	95.39	67.40	19.96	0.83	0.02	0.01	0.07	3.92	0.02	0.29	0.02	8.09
JLN-S3-15	110–120	5.98	0.59	13.93	94.42	67.96	19.61	1.00	0.03	0.01	0.06	3.83	0.01	0.30	0.02	7.93
JLN-S4-01	0–5	12.97	2.12	27.83	97.63	70.37	16.08	0.25	0.02	0.03	0.09	4.31	0.01	0.30	0.02	9.25
JLN-S4-02	5–10	7.88	1.08	20.77	98.02	71.15	16.35	0.24	0.02	0.02	0.09	4.34	0.01	0.28	0.02	8.09
JLN-S4-04	15–20	9.00	0.39	7.60	98.11	60.14	23.18	0.34	0.02	0.02	0.12	5.84	0.01	0.41	0.02	10.58
JLN-S4-05	20–25	7.41	0.74	15.58	97.99	65.17	20.35	0.29	0.02	0.02	0.11	5.18	0.01	0.35	0.02	9.11
JLN-S4-07	30–40	7.23	0.21	4.68	98.01	62.94	22.23	0.32	0.02	0.03	0.11	5.49	0.01	0.38	0.02	9.81
JLN-S4-09	50–60	6.78	0.13	2.59	98.12	66.81	19.88	0.29	0.02	0.01	0.09	4.86	0.01	0.34	0.02	8.51
JLN-S4-12	80–90	6.84	0.08	1.57	98.29	66.48	20.28	0.27	0.02	0.01	0.07	4.76	0.01	0.34	0.02	8.77
JLN-S4-15	110–120	6.20	0.09	1.90	98.32	65.69	20.86	0.27	0.02	0.01	0.09	4.64	0.01	0.34	0.02	8.91

TOC content (Table 4 and Fig. 3) varies between 0.12 and 3.93 wt.% C, showing an increasing tendency upward in all the profiles. Also TOC content generally decreases for comparable depths from the foot to the hilltop.

3.2. Major mineral composition of the soil and weathering profiles

Major mineral composition data of the profiles are presented in Table 5 and their variations versus profile depth are plotted in Fig. 4. The granitic regolith studied is composed of quartz, feldspars (K-feldspar and plagioclase), mica and chlorite as the primary minerals, with kaolinite and gibbsite as weathering products. Mineral composition in the profiles varied with weathering extent and stages.

Quartz content varies between 26 and 90 wt.% in the profiles. Quartz content in samples below 400 cm increases slightly upward in the profile whereas above this depth, the quartz content shows a fast increase to the depth of 200 cm and then there is a rapid decrease upward in JLN-S1. The upper meter sampled in the other three profiles shows large variations in quartz content (Fig. 4 and Table 5).

Table 4
Total organic carbon (TOC) content of profile samples.

Sample no.	Depth (cm)	TOC (%)	Sample no.	Depth (cm)	TOC (%)	Sample no.	Depth (cm)	TOC (%)	Sample no.	Depth (cm)	TOC (%)
JLN-S1-01	0–20	3.93	JLN-S2-01	0–5	3.68	JLN-S3-01	0–5	1.80	JLN-S4-01	0–5	1.25
JLN-S1-02	20–30	1.35	JLN-S2-02	5–10	1.91	JLN-S3-02	5–10	0.68	JLN-S4-02	5–10	0.49
JLN-S1-03	30–40	0.86	JLN-S2-03	10–15	1.84	JLN-S3-03	10–15	0.50	JLN-S4-03	10–15	0.38
JLN-S1-04	40–50	0.66	JLN-S2-04	15–20	1.02	JLN-S3-04	15–20	0.38	JLN-S4-04	15–20	0.41
JLN-S1-05	50–60	0.51	JLN-S2-05	20–25	0.91	JLN-S3-05	20–25	0.28	JLN-S4-05	20–25	0.23
JLN-S1-06	60–70	0.46	JLN-S2-06	25–30	0.47	JLN-S3-06	25–30	0.30	JLN-S4-06	25–30	0.18
JLN-S1-07	70–80	0.28	JLN-S2-07	30–40	0.36	JLN-S3-07	30–40		JLN-S4-07	30–40	0.19
JLN-S1-08	80–90	0.24	JLN-S2-08	40–50	0.27	JLN-S3-08	40–50	0.26	JLN-S4-08	40–50	0.15
JLN-S1-09	90–100	0.23	JLN-S2-09	50–60	0.35	JLN-S3-09	50–60	0.22	JLN-S4-09	50–60	0.22
JLN-S1-10	100–110	0.20	JLN-S2-10	60–70	0.20	JLN-S3-10	60–70	0.19	JLN-S4-10	60–70	0.17
JLN-S1-11	110–120	0.20	JLN-S2-11	70–80	0.16	JLN-S3-11	70–80	0.33	JLN-S4-11	70–80	0.23
JLN-S1-12	120–130	0.23	JLN-S2-12	80–90	0.19	JLN-S3-12	80–90	0.16	JLN-S4-12	80–90	0.13
JLN-S1-13	130–140	0.20	JLN-S2-13	90–100	0.19	JLN-S3-13	90–100	0.15	JLN-S4-13	90–100	0.14
JLN-S1-14	140–150	0.22	JLN-S2-14	100–110	0.19	JLN-S3-14	100–110	0.15	JLN-S4-14	100–110	0.12

In the weathering profile of JLN-S1, the K-feldspar content is relatively constant (30–45 wt.%) versus depth below 400 cm and then decreased sharply to as low as 2 wt.% from the depth of 400 cm upward (Fig. 4 and Table 5).

In the deepest profile, plagioclase decreases consistently upward to the depth of 550 cm at which point no plagioclase was present. The predominant clay mineral is kaolinite and gibbsite in the studied profiles. Kaolinite contents increase from 4 wt.% at 1100 cm depth to 10 wt.% at 400 cm in JLN-S1. The samples above 400 cm showed a slight decrease in kaolinite contents to the surface of the weathering profile. Gibbsite contents generally rise from 0 wt.% at the bottom of JLN-S1 to 3 wt.% at the top of it, except for occasional anomalously high values at depths of about 370 cm and 570 cm. In general, gibbsite is found above 400 cm in the weathering profile. The hilltop soil profile JLN-S4 has the highest gibbsite content (5–8 wt.%), nearly twice that of the profiles down the slope. Chlorite appears in both bedrock and profile samples at a relatively stable concentration of about 3 to 6 wt.% (Table 5).

In contrast to the middle and bottom profiles, no K-feldspar is detected in the top soil profile JLN-S4. In addition, the kaolinite and gibbsite contents of JLN-S4 (8–14 wt.% and 5–8 wt.%) are generally higher than the middle and bottom slope profiles (6–16 wt.% for kaolinite and 2–3 wt.% for gibbsite) (Fig. 4 and Table 5).

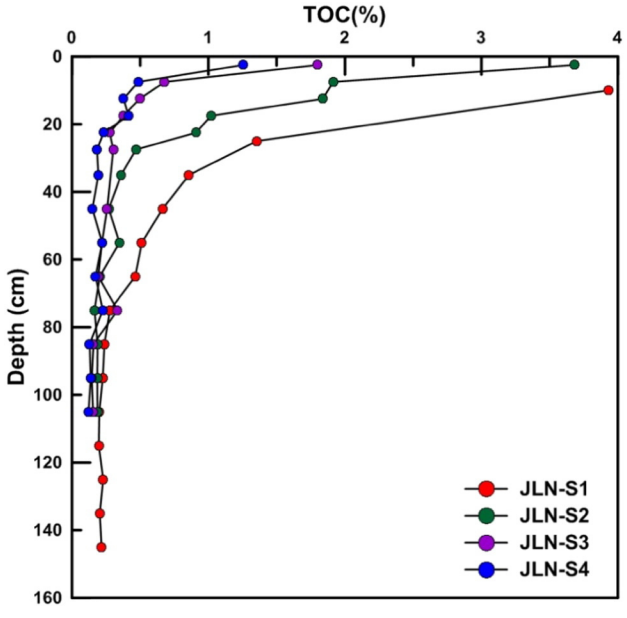

Fig. 3. Total organic carbon (TOC) content plotted versus depth for the four profiles as shown in legend.

3.3. Major chemical composition of the soil and weathering profiles

Interpretation of parent composition is typically the most difficult choice in a weathering study because parent composition can change and can never be definitely inferred. One bedrock sample, JLN-R3, was selected as the best sample of fresh parent rock for the profiles because of its low LOI, its mineral type and texture similarity with the bottom samples of the weathering profile. The CIA value of JLN-R3 is 49.99, which is in the range of fresh granite and granodiorites (Nesbitt and Young, 1982). JLN-R3 was used to normalize the mineralogy and element alteration of the profiles. Standard of deviation calculation for the major elements of the four bedrock samples are given in Appendix B. Zr and Ti are commonly chosen as inert elements in previous studies where element mobility has been calculated (Nesbitt, 1979; Brimhall and Dietrich, 1987), for they both reside in weathering resistant minerals such as zircon and rutile respectively. For Ti, even though rutile weathers, it readily forms the insoluble Ti-oxides and Fe–Ti-oxyhydroxides (Nesbitt, 1979). Some researchers have argued, however, that Zr is generally more inert in granitic profiles than Ti. Other than geochemical mobility, heterogeneity of the inert element in the parent material should be assessed to avoid inter-sample error when calculating the PERC. CHANGE of a mobile element. For the granite bedrock samples, zircon is more likely to be distributed uniformly, while Ti is less likely to be subjected to this issue as it is much more abundant than Zr as a major element (Nesbitt, 1979). Coefficients of variation for Zr and Ti contents in the four bedrock samples are 0.12 and 0.08 respectively (Zr content data from Liu, 2013 and Zhang et al., 2015). So, Ti was assumed to be a better candidate for inert element in this study.

The major chemical compositions of bulk samples (Table 3) were normalized with respect to Ti (bedrock JLN-R3) and are plotted with profile depth in Figs. 5 and 6. In the profiles, all the major elements show different extents of depletion compared to the bedrock samples, except for Fe in the upper part of the profiles. Fe becomes depleted during the incipient weathering stage of granite, but became enriched in the upper part of the weathering profile and all soil profiles.

Si and Al generally become depleted as weathering proceeds above 200 cm and 100 cm respectively. LOI which indicates H_2O and organic content in weathering product and soil presents an obvious increasing trend upward the profiles.

4. Discussion

4.1. Mineral weathering reactions and element variations

4.1.1. Staged weathering reactions and cation release

Granite rock is composed of minerals with different resistances to weathering. This has been noted since publication of the Goldich chemical weathering stability series (Goldich, 1938). The overall trends of mineral

Table 5
Major mineral composition of weathering and soil profiles.

Sample no.	Depth (cm)	Quartz (wt.%)	K-feldspar (wt.%)	Plagioclase (wt.%)	Kaolinite (wt.%)	Gibbsite (wt.%)	Chlorite (wt.%)	Sepiolite (wt.%)	Mica (wt.%)	Other minerals (wt.%)
JLN-S1-1	0–20	35	5	0	7	3	?	5	4	
JLN-S1-2	20–30	45	2	0	8	3	5	5	4	
JLN-S1-3	30–40	26	7	0	8	3	4	0	0	
JLN-S1-4	40–50	42	2	0	7	3	0	0	0	
JLN-S1-5	50–60	51	3	0	7	3	5	0	0	
JLN-S1-7	70–80	60	2	0	6	2	0	0	0	
JLN-S1-9	90–100	80	4	0	6	2	5	0	0	
JLN-S1-11	110–120	67	2	0	7	2	0	0	0	
JLN-S1-13	130–140	66	3	0	7	2	?	0	4	
JLN-S1-15	150–160	45	4	0	9	2	6	6	4	
JLN-S1-15	150–160	48	3	0	8	2	4	0	0	
JLN-S1-17	170–180	90	2	0	4	1	0	0	0	
JLN-S1-18	180–190	90	2	0	5	1	0	0	0	
JLN-S1-19	190–200	69	7	0	7	1	?	6	0	
JLN-S1-20	200–220	55	6	0	8	1	0	0	?	
JLN-S1-21	220–240	73	3	0	6	0	0	0	0	
JLN-S1-23	260–280	61	7	0	8	1	0	0	4	
JLN-S1-24	280–300	74	8	0	7	1	?	4	?	
JLN-S1-25	300–320	47	6	0	7	2	0	0	4	
JLN-S1-26	320–340	59	12	0	8	0	0	?	0	
JLN-S1-28	360–380	41	24	0	9	5	?	6	5	
JLN-S1-29	380–400	42	36	0	9	2	5	0	?	
JLN-S1-30	400–420	42	30	0	10	2	5	5	5	
JLN-S1-33	460–480	45	26	0	8	0	4	?	5	
JLN-S1-36	520–540	50	35	0	6	2	0	0	4	
JLN-S1-37	560–580	40	28	2	8	5	6	6	5	
JLN-S1-41	640–660	41	33	3	6	2	5	5	4	
JLN-S1-44	700–720	36	41	10	5	0	0	0	4	
JLN-S1-47	760–780	36	32	4	7	0	6	6	5	
JLN-S1-50	850–900	40	36	4	6	?	5	4	?	
JLN-S1-51	900–950	32	44	8	7	0	6	0	0	
JLN-S1-52	950–1000	40	30	12	5	0	6	5	0	
JLN-S1-53	1000–1100	38	30	15	4	0	4	4	3	
JLN-R1		30	20	25	7	0	6	5	3	
JLN-R2		18	18	28	2	0	4	4	15	Hornblende 3
JLN-R3		16	25	27	3	0	3	0	10	Hornblende 5
JLN-R4		32	20	29	3	0	5	5	3	
JLN-S2-1	0–5	62	2	0	10	3	5	5	0	
JLN-S2-2	5–10	55	1	0	10	3	6	6	0	
JLN-S2-3	10–15	46	1	0	10	3	5	0	0	
JLN-S2-5	20–25	43	1	0	11	3	5	5	0	
JLN-S2-7	30–40	45	1	0	11	3	6	6	0	
JLN-S2-9	50–60	49	1	0	12	3	4	0	0	
JLN-S2-10	60–70	75	1	0	10	2	5	4	0	
JLN-S2-13	90–100	44	1	0	16	2	6	5	4	
JLN-S2-15	110–120	68	2	0	10	2	5	0	0	
JLN-S3-1	0–5	51	1	0	8	3	5	5	0	
JLN-S3-2	5–10	31	2	0	9	3	6	5	0	
JLN-S3-3	10–15	49	2	0	11	3	4	0	3	
JLN-S3-5	20–25	49	1	0	8	2	?	0	0	
JLN-S3-7	30–40	70	1	0	11	3	6	5	0	
JLN-S3-9	50–60	56	6	0	11	2	?	0	0	
JLN-S3-12	80–90	60	1	0	11	2	0	4	4	
JLN-S3-15	110–120	36	1	0	8	3	6	6	4	
JLN-S4-1	0–5	62	0	0	9	6	6	5	0	
JLN-S4-2	5–10	61	0	0	8	6	4	0	0	
JLN-S4-4	15–20	31	0	0	13	8	6	5	0	
JLN-S4-5	20–25	42	0	0	10	6	6	6	0	
JLN-S4-7	30–40	37	0	0	11	7	5	0	0	
JLN-S4-9	50–60	46	0	0	10	5	5	0	0	
JLN-S4-12	80–90	47	0	0	12	5	6	6	0	
JLN-S4-15	110–120	42	0	0	14	5	5	0	0	

and element variation in the deep weathering profile JLN-S1 document stages in the weathering process of the granite bedrock, i.e., reaction fronts related to dissolution of different primary minerals. These stages are documented by the variations in the physical and chemical characteristics (pH, CEC, BS, grain size, element concentrations).

To interpret weathering first requires the assumption of a reasonable parent composition. As shown in Fig. 5, the bedrock chosen as parent yields a reasonable estimate of parent when considered with the entire dataset. In other words, for the most concentrated elements, the variation of the bedrock is relatively small and these values bracket much of the data from the deepest depths in the JLN-S1 profile (i.e., Si, K, Na, Fe, Mn, LOI). In contrast, the variations in other elements (Ca, Mg, P, Al) are much larger and probably indicative of variation in abundance and/or extent of weathering of the accessory minerals hornblende (Ca, Mg, Al) and apatite (P). Both of these minerals have been observed to weather deep in a profile in the weathered rock in another granitic rock tropical weathering site (Buss et al., 2008).

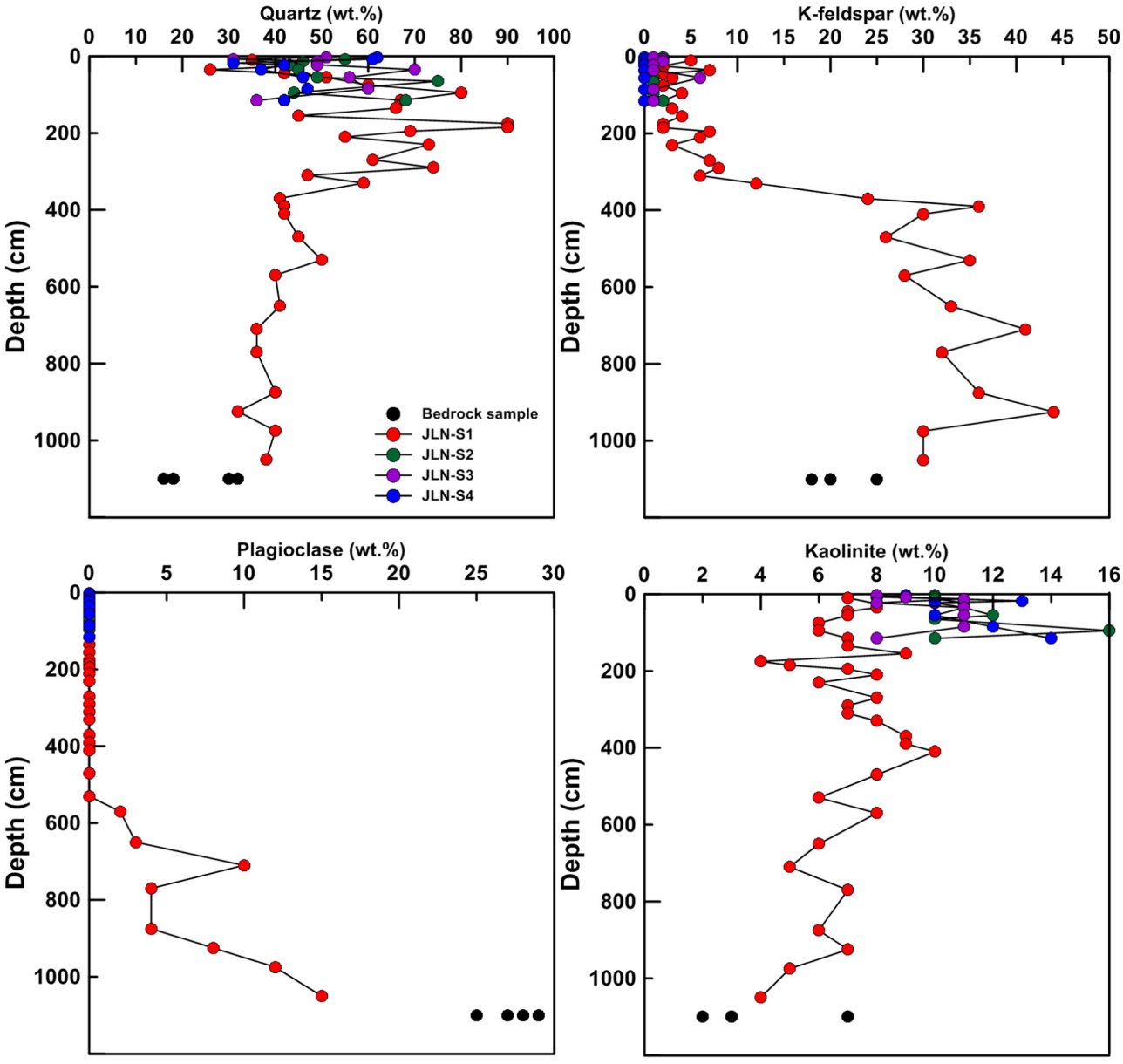

Fig. 4. Concentrations of major minerals plotted versus depth for all profiles as indicated in the legend in the first panel.

4.1.1.1. Mica, hornblende and plagioclase reaction front. In the bedrock sample JLN-R3, the mica and hornblende composition is 10 wt.% and 5 wt.% respectively (Table 5). The large variability in Ca, Al, and Mg contents of the rock samples (Fig. 5) is attributed to early weathering of biotite and hornblende. Using this assumption and the mineralogy based on the X ray diffractograms, we infer that during this earliest initial stage of weathering from fresh bedrock to the bottom sample of weathering profile JLN-S1, the mica content decreased from 10 wt.% to 3 wt.% and hornblende decreased from 5 wt.% to below detection (Table 5). It is common to observe in granites that these Fe-containing minerals are the most reactive minerals because they start reacting and become depleted at the very beginning of the chemical weathering process (Buss et al., 2008; Navarre-Sitchler et al., 2015). Furthermore, Buss et al. (2008) have argued that oxidation of biotite is the first reaction to occur in some granitic rocks in the presence of O_2-charged meteoric waters. Oxidation of the biotite is accompanied by loss of K to maintain charge balance.

The plagioclase content also drops (from 27 wt.% to 15 wt.%) at great depth: specifically, the depletion occurs between 1100 and 550 cm. Depth intervals where individual minerals become depleted are interpreted as zones where they dissolve and are therefore referred to as reaction fronts. The depletions in mica, hornblende and plagioclase content document that reaction fronts of these minerals occur at the deepest depths, and that the Fe-containing minerals weather the earliest. The reaction front for K-feldspar (discussed below) occurs at much shallower depths. Previous studies reported similar differences in weathering resistance for K-feldspar versus plagioclase (Nesbitt and Young, 1984; White et al., 2001; Navarre-Sitchler et al., 2015).

Ti-normalized depth profiles for Ca, Mg, Al and P are difficult to interpret because the variability in the rock samples is large (Fig. 5). We infer that up to 90% of the Ca is lost at the bedrock-weathered rock interface, and a smaller amount is lost from 1100 to 600 cm. This could be interpreted as documenting early dissolution of accessory hornblende (very near 1100 cm) followed by a wide reaction front for a low-anorthite plagioclase (from 1100 to 600 cm). Loss of Ca is also attributed to dissolution of minor calcite (White et al., 1999) as well as dissolution of apatite, which is the dominant P-containing mineral (Middelburg et al., 1988). Although no apatite was detected by XRD, we infer that the resolution of XRD is too low and that the P contained in the rock is nonetheless present as apatite (Table 3),

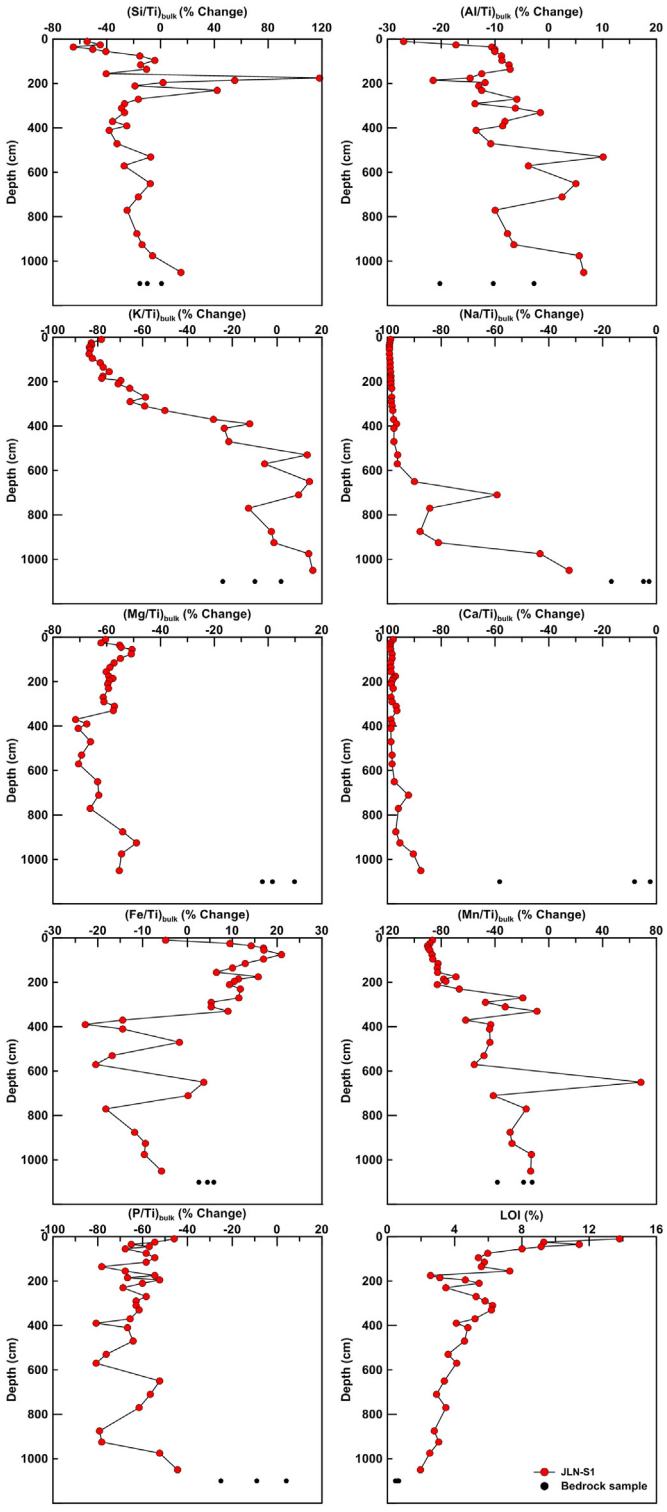

Fig. 5. PERC. CHANGE of major elements (Ti normalized) and values for Loss on Ignition (LOI) plotted versus depth for profile JLN-S1 and for bedrock samples. See text for information about PERC. CHANGE calculation.

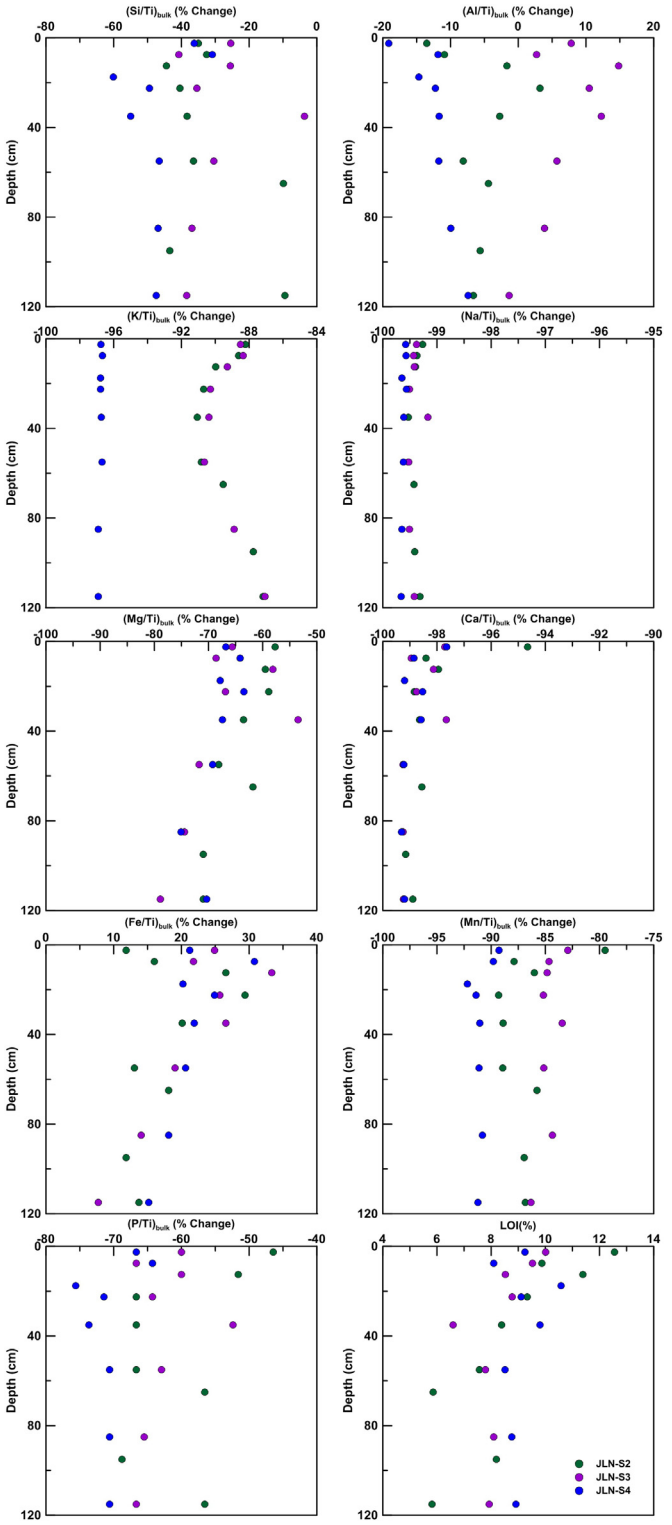

Fig. 6. PERC. CHANGE of major elements (Ti normalized) and values for Loss on Ignition (LOI) plotted versus depth for the three soil profiles JLN-S2, S3, S4.

perhaps with minor monazite. One interpretation of P variation in Fig. 5 is that significant loss of P occurred at the bedrock-weathered rock interface (documented by variability in rock composition compared to the weathered material) and retention of P either as an insoluble mineral such as monazite or absorbed species on iron oxides.

4.1.1.2. K-feldspar reaction front. During chemical weathering, while plagioclase dissolves at great depth, K-feldspar is relatively resistant (Nesbitt et al., 1980; Middelburg et al., 1988). The plagioclase content was as high as 27 wt.% in the bedrock. During the plagioclase-dominated weathering stage (below 550 cm in JLN-S1), the significant depletion in plagioclase content could explain why weathering-resistant

minerals such as quartz increase in concentration over some depths (Fig. 4). In contrast, the K-feldspar content is roughly constant from 1100 to 400 cm but then decreases above 400 cm, with an especially sharp depletion between 400 and 200 cm. K PERC. CHANGE decreases sharply from about 0 at the depth of 550 cm to −80% at the depth of 200 cm. The Ti normalized percentage variation of K though the JLN-S1 profile shown in Fig. 5 documents the K-feldspar reaction front from 550 cm to 200 cm. From 200 cm upward, K-feldspar content stays in a narrow range at about 6–9 wt.% and the depletion of K stays at about −80%.

4.1.1.3. Quartz reaction front. Quartz shows an increase from 1100 cm upward to 200 cm (Fig. 4). Over most of the profile, dissolution of feldspar dominates the granite weathering in JLN-S1, explaining the relative enrichment of quartz in Fig. 4. Based on the quartz and Si PERC. CHANGE variations in JLN-S1 profile, 200 cm depth is the bottom of the quartz weathering reaction front; in other words, quartz starts to be removed out of the weathering system above that depth (Figs. 4, 5). However, significant fragmentation of quartz is inferred from the grain size variation (Fig. 2) and field observations indicate that vertical transport of fine particles of quartz down the profile should also be considered as a potential factor affecting the weathering profile for Si.

4.1.1.4. Kaolinite and gibbsite formation. Kaolinite and gibbsite are the main secondary minerals in the profiles, with kaolinite dominant. Kaolinite is the typical product of intensive weathering of feldspar in tropical and sub-tropical areas where the extent of reaction does not proceed all the way to gibbsite, particularly on acidic rocks in well-drained and temperate environments. Gibbsite can also form as a major end-product of aluminosilicate mineral weathering if time and conditions allow (Sequeira Braga et al., 2002).

Fig. 4 documents a general increase in kaolinite in the JLN-S1 profile from about 4 wt.% in the bottom sample to 10 wt.% at 400 cm. Above 400 cm, the kaolinite content slightly decreases to 7–8 wt.% where it stays constant at shallower depths. In one horizon at 170–190 cm where we observed a quartz vein in the original granite, the kaolinite content was lower (4–5 wt.%). As discussed above, from bedrock to the depth of 550 cm plagioclase is dissolving and from 550 cm upward to 200 cm K-feldspar is dissolving. The continuously increasing kaolinite content during the granite weathering is thus attributed to feldspar weathering.

In profile JLN-S1, gibbsite increases upward in the profile above 400 cm (Table 5), a depth which coincides with the depth where kaolinite begins decreasing. It is reasonable to assume that 400 cm is the bottom of the reaction front where kaolinite transforms to gibbsite. So, kaolinite variation above 400 cm is not only influenced by feldspar weathering, but also by desilication and conversion of kaolinite into gibbsite, releasing Si from the profile. Consistent with this, the <2 μm fraction, which is typically assumed to be dominated by clay minerals in previous research (Bengtsson and Stevens, 1998; Hassellöv et al., 2001; Pehlivanoglou et al., 2004), increases constantly upward from the depth of 400 cm (Fig. 2).

For the profile samples with CIA < 85 (i.e., below 360 cm), the Si/Al values are negatively correlated with CIA (Fig. 7). As weathering proceeds, feldspars weather and clay minerals form, resulting in a decreasing Si/Al ratio (Robert and Tessier, 1992). No obvious relationship with CIA and stoichiometric release of Si and Al are observed for the samples above 100 cm (Fig. 7). The relatively stable and low feldspar contents, in addition to the variations in kaolinite contents between 6 and 8 wt.% (Fig. 4 and Table 5), indicate that feldspar weathering is not the dominant control on the Si/Al ratio for samples above 360 cm. From the grain size variation along the weathering profile (Fig. 2), the decrease in the 20–2000 μm fractions and the synchronous increase in the <2 μm and 2–20 μm fractions from 400 cm upward are consistent with both fragmentation of primary minerals and formation of secondary minerals. Downward transport of fine particles of quartz and K-feldspar in the upper part of the profiles might also contribute to the Si/Al ratio variations. Low pH values (below 5), organic ligands and degree of fragmentation (Figs. 2 and 3) all can promote the dissolution of quartz and K-feldspar, as well as the kaolinite–gibbsite transformation, therefore impacting the Si/Al ratio variation in this upper zone of the profile.

The dominant reactions according to the mineral and major element variations are summarized below (the left side of each formula is the mineral in the weathering profile or bedrock; the right side of each formula summarizes the secondary product and released cations; no attempt is made to balance the reactions). A weathering reaction sequence and the approximate depth for reaction boundaries in the weathering profiles JLN-S1 are delineated in Fig. 8:

I. Apatite → $Ca^{2+} + PO_4^{3-}$
II. Plagioclase → kaolinite + $H_4SiO_4 + Na^+ + Ca^{2+}$

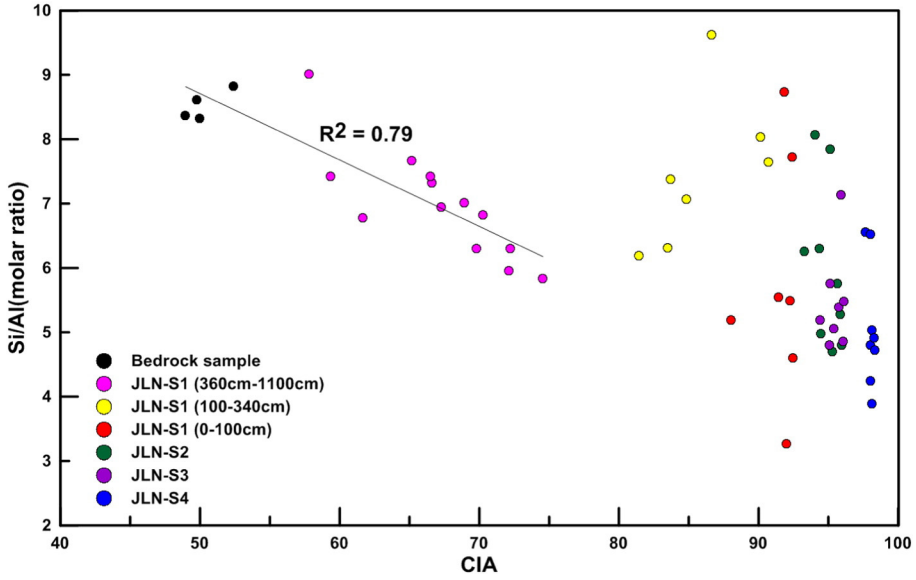

Fig. 7. Variation in Si/Al molar ratio plotted versus the calculated CIA for the four profiles and bedrock samples, as indicated in legend. A regression equation is shown for the data for the samples below 360 cm depth in JLN-S1 profile plus bedrock.

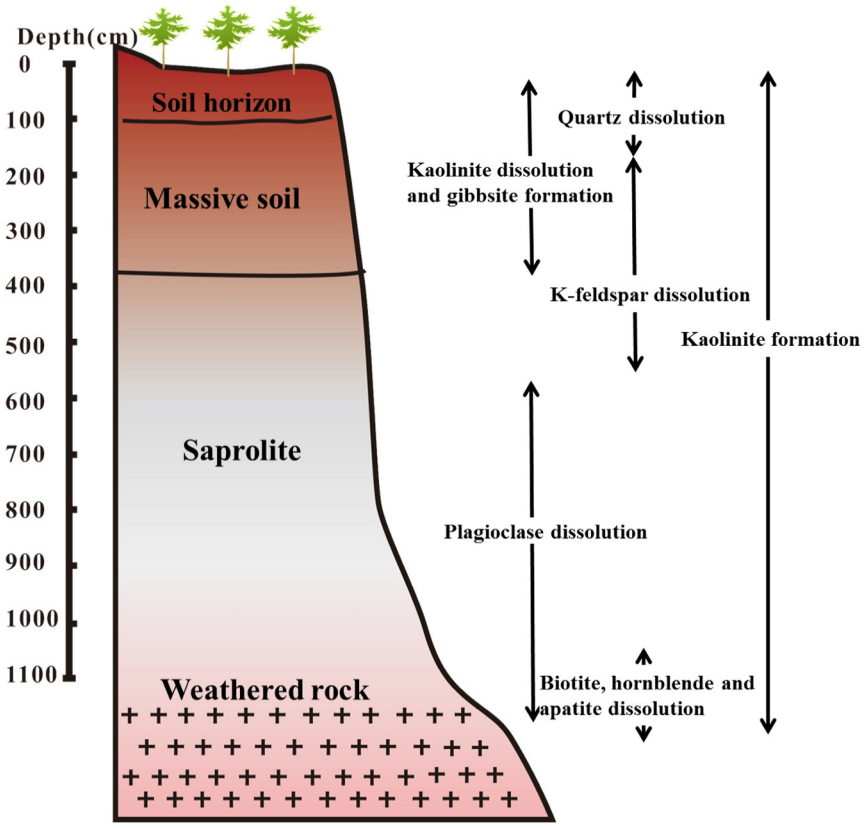

Fig. 8. Schematic figure showing the zonation in the weathering reaction sequence and the approximate depths for reactions in profile JLN-S1. The weathered rock zone is characterized by dissolution of biotite, hornblende, and apatite, and initiation of plagioclase dissolution; the saprolite zone is dominated by plagioclase dissolution and initial K-feldspar dissolution; the massive soil is dominated by later stage of K-feldspar weathering and clay mineral transformation; the soil zone is where quartz is observed to be the dominantly dissolving primary mineral and where obvious bio-turbation is noted. The crosses symbolize the fresh granite bedrock. The solid lines in the profile at about 400 cm and 100 cm depth indicate the boundary of saprolite, massive soil and soil.

III. Biotite → kaolinite + H_4SiO_4 + Mg^{2+} + K^+ + Fe^{2+} + Fe oxide
IV. Hornblende → kaolinite + H_4SiO_4 + Ca^{2+} + Na^+ + Mg^{2+} + Fe^{2+} + Fe oxide
V. K-feldspar → kaolinite + H_4SiO_4 + K^+
VI. Kaolinite → gibbsite + H_4SiO_4
VII. Quartz → H_4SiO_4.

4.1.2. Plant nutrient element evolution on the upper horizon of weathering profiles

The reactions in Fig. 8 explain much of the element variations in the profiles. Feldspar transforming to clays accounts predominantly for alkalis and alkaline earth release from the profile (except for Mg), and also accounts for much of the Si and Al loss. Fe-containing minerals weather earliest, and are followed by plagioclase weathering, followed by K-feldspar. Accessory mineral weathering dominantly explains the Mg, Mn and P release at the early weathering stage. However, there are other environmental factors like redox conditions, biological uptake etc., which are likely important in the weathering profile.

As variable valence elements, Fe and Mn are controlled not only by the weathering of their dominant host mineral but also by the redox and drainage conditions through the profile (Driese, 2004) and biological activity. For example, Fe variations were similar to Mn in the weathering stage below 400 cm depth (Fig. 5). From the bottom up in the JLN-S1 profile, the PERC. CHANGES of Fe and Mn show a decreasing tendency as weathering proceeds except for a few anomalies. The anomalies are likely related to variations in Mn- and Fe-hosting minerals in the protolith granite. However, above 400 cm, the two elements show some discrepancy.

For example, the Fe PERC. CHANGE increases from about −20% around 400 cm depth to +20% at around 100 cm and then decreases constantly to about −5% in the surface sample of JNL-S1 (Fig. 5). To first approximation, then, Fe is largely retained in this weathered profile. However, variations in Fe content with depth are well known to occur due to movement of the Fe within a profile (Fimmen et al., 2008). As an essential nutrient for plants, active bio-pumping by vegetation might be an explanation for concentrated Fe in the shallow horizons of the profile. In bio-pumping, plants uptake Fe from the profile into roots and give the mineral nutrient back to the profile at the land surface after decaying. Unlike K, Ca, and Mg that are readily transported out of the profile by soil solutions, Fe may be concentrated as insoluble secondary Fe oxides as the profile develops (White et al., 2008). In addition, above 100 cm, the high TOC content (Table 4. and Fig. 3) documents strong biological activity, perhaps also driving some Fe reduction in this zone. In that case, Fe^{3+} would be reduced to Fe^{2+}, which then could be released from the profile (Chesworth, 1992). Alternately, organic complexation of Fe(III) can also remove Fe from a weathering system (Millero et al., 1995; McKnight et al., 2001; Brantley et al., 2014; Fujii et al., 2014). Thus, Fe may be mobilized from upper layers of the profile and then be oxidized at depth, or the organic ligand may be decomposed at depth, causing Fe enrichments in the subsurface: this conceptual model may explain the maximum enrichment factor of nearly 20% at about 100 cm depth. The ratio of oxidant supply to the rate of acid supply is the key factor controlling the release or retention of Fe in the weathering profile (Holland and Zbinden, 1988).

In contrast to the Fe-enrichments in the upper layers of the profile, Mn PERC. CHANGE shows a peak in the 270–400 cm depth interval and then decreases upward to about −90% at around 200 cm. In other words, 90% of the Mn in the upper layers is depleted with respect to

the bedrock. Similar to Fe, the behavior of Mn is generally controlled by organic complexation, redox and biological activity. Mn(II) is easily mobilized into solution, while Mn(IV) tends to reside in oxide or hydroxides which are nearly immobile (Holland and Zbinden, 1988). It is reasonable to ascribe the concentrated Mn in the depth interval from about 270 to 400 cm to loss of Mn from the upper layers due to organic complexation or bacterial reduction reactions, decomposition of organic ligands and oxidation of the Mn followed by precipitation of Mn(IV) oxides or hydroxides. Loss of Mn from deeper depths can be attributed to loss of the more soluble Mn(II) species under more reducing conditions at depth.

The different depths of retention or depletion for Fe and Mn could result from differences in their redox properties, solubilities as a function of oxidation state, differences in vegetation uptake, and differences in weathering products. More comprehensive illumination of Fe and Mn oxide dissolution, organic complex leaching and biotic accumulation is beyond the scope of this paper.

P is also a macronutrient for plants. The profile is inferred to have lost about 60% of the P at the early weathering stage presumably due to apatite dissolution. P PERC. CHANGE stayed at about −60% in the profile, increasing slightly to the surface. The relatively constant P content is most likely because i) a second primary mineral such as monazite contains P in the bedrock and is retained even when apatite is dissolved away, and/or ii) P is absorbed tightly to iron oxides in the weathered profile. Growing vegetation also likely takes up P and then decays and releases it back to the profile over time.

4.2. Lateral movement of soil materials along the hillslope

Lateral movement of weathering products down the ridgeline transect is inferred from the concentrations of the more resistant minerals K-feldspar and quartz, and possibly from the TOC contents (Figs. 3, 4, 5 and 6). Specifically, a continuous increase in K-feldspar content and K PERC. CHANGE is observed from the top to the middle soil profiles and to the upper 120 cm of the bottom weathering profile (Figs. 4, 5 and 6) at the slope bottom. The K-feldspar and K PERC. CHANGE variations show slightly increasing trends toward the surface in individual profiles compared with the lower section (Figs. 4 and 5). We interpret these data to document transport of relatively weathering resistant K-feldspar from the upper hill down the slope. Quartz is another resistant mineral that may be accumulating due to solid material transport along the hillslope. The middle profiles JLN-S2 and JLN-S3 have higher contents of the quartz and increased Si PERC. CHANGE in both profiles (Figs. 4 and 5). However, the upper 120 cm horizon of JLN-S1 at the hill bottom does not show an obvious accumulation of quartz, Si and Al compared with the middle profiles. Quartz content is at least one magnitude higher than K-feldspar in the soil profiles (Table 5), so compared with K-feldspar, the extent of quartz particles transported down the slope might be concealed by the high content of quartz in the soil or analyzing errors.

TOC content also shows an obvious increasing trend from the hill top profile JLN-S4 to the middle slope profiles JLN-S3, JLN-S2 and the lowest hill weathering profile JLN-S1 (Fig. 3). As the dominant factor controlling soil pH (Chesworth, 1992), the accumulation of organic matter along the hill slope is reflected in the pH variation between the different profiles (discussed later in Section 4.3). At a depth of about 100 cm, the TOC contents for all four profiles are similar and very low (from 0.14% to 0.23%). Below this depth, TOC remains stable at about 0.22% in JLN-S1 downward until the deepest measured 150 cm sample. Organic matter is soluble and easily transported with weathering fluid down the slope and in the individual profile. Considered together with bio-pumping and the feedbacks discussed for nutrient elements in the JLN-S1 profile in Section 4.2, 100 cm is believed to be the lower boundary of most active pedogenesis for the profiles (Fig. 8). This depth is also inferred to be the maximum horizon depth at which lateral movement of materials down the slope could be detected.

4.3. Evolution of pH in terms of weathering reactions and lateral movement

The measured pH values at a given depth for the JLN-S1, S2 and S3 profiles down along the hill-ridge increased. TOC and pH are plotted in Fig. 9, showing an obvious negative relationship. We infer that organic matter is the dominant factor or a correlative factor controlling pH in each soil horizon. For example, CO_2 released through root respiration and organic matter degradation in soil can increase P_{CO_2} in the soil atmosphere two orders of magnitude higher than atmospheric P_{CO_2}. The pH can equal approximately 5.7 at equilibrium with atmosphere P_{CO_2}, but can be as low as 4.5 at the higher P_{CO_2} values in the soil atmosphere (Chesworth, 1992). We infer that TOC transported down the hillslope or TOC accumulated at the lower elevations due to less drainage could be the explanation for the decreasing trend of pH from middle soil profiles to the bottom. However, the pH measured in the top profile JLN-S4 is lower than those measured in the middle profiles, and is closer to measured values in the bottom profile JLN-S1 (Fig. 2), even though it has the lowest TOC content. This is likely due to the fact that this uppermost profile is highly depleted in primary minerals as discussed below.

The pH values in the four profiles are plotted along with BS in Fig. 9. A positive relationship is observed for the JLN-S1 samples below the soil horizon. This is attributed to the effect of proton consumption during weathering of primary silicates. For the middle profiles JLN-S2, S3 and the soil horizon of JLN-S1, organic acid accounts for most of the acidity and H^+ balances most of the negative charge in the soil, resulting in

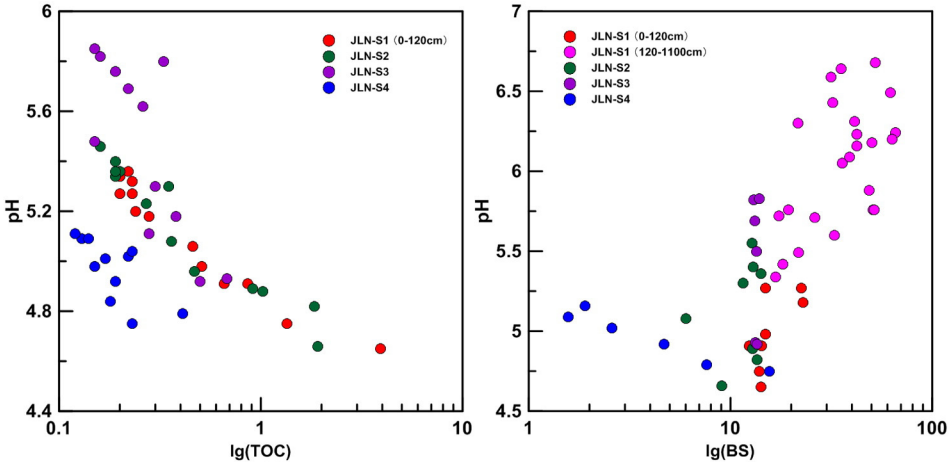

Fig. 9. pH in the four profiles plotted versus TOC (left panel) and base saturation (right panel).

low BS values. However, K-feldspar and occasionally mica are observed in the soil horizons of JLN-S1 and JLN-S2, S3 (Fig. 4 and Table 5). Those primary silicates weather in the low pH conditions and release base cations to the profile, maintaining BS relatively stable around 10% (Figs. 2 and 9). Lacking base cations from weathering of primary silicates, Al^{3+} and H^{+} are inferred to become the dominant exchangeable cations in the top profile JLN-S4, resulting in low pH compared to the soil horizons down slope.

The hilltop soil profile JLN-S4 shows a negative relationship between pH and BS. The depletion of primary silicates like feldspar and mica (Fig. 4 and Table 5) in JLN-S4 means that this profile has low base cation content, and thus a low BS value. The atmospheric cation input could also have some impact on BS as this is a source of exchangeable base cations. In the middle and bottom profiles where cation release from primary silicate weathering is intense, the atmospheric impact on BS could be relatively insignificant. However, the depletion of primary silicates in the top profile means that the contribution from atmospheric cations may be relatively important as a contribution to the exchangeable base cation pool. So BS decreases down the profile while the pH increases following the decrease in organic matter content (Fig. 3).

4.4. Mass balance calculations along the granite hillslope catena

A mass balance model was proposed for hillslope evolution at the Susquehannna/Shale Hills Critical Zone Observatory (Jin et al., 2010) following a previous model by Yoo et al. (2007). In that study, the model was applied to the augerable soil. Here, we use the model on the upper 120 cm by assuming that layer represents the mobile soil. In contrast to Jin et al. (2010) where the target hillslope was a planar interfluve hillslope, here the model is used to treat a ridgeline that parallels a channel (Fig. 1). We use this model simply as a way to quantitatively calculate mass balance on the hillslope positions given a simple steady-state model.

The denudation rates of the four studied profiles were calculated from cosmogenic nuclide measurements (^{26}Al, ^{10}Be) in another study (Cui, 2014): for JLN-S1, S2, S3, S4 the rates are 19 ± 2 m/Ma, 40 ± 3 m/Ma, 48 ± 3 m/Ma and 21 ± 1 m/Ma respectively. Thus, for JLN-S1, the profile thickness (1100 cm) divided by denudation rate (19 ± 2 m/Ma) yields an estimated weathering profile residence time of 0.58 Ma. Likewise for the upper 120 cm horizon in the different sites, the residence time is less than 0.06 Ma, about only 1/10 of the weathering time estimated by JLN-S1. Both of the time periods are much shorter compared with the age of the granite complex (178.2 ± 0.84 Ma, Fan and Chen, 2000) as expected.

Glacial activity is a possible erosional perturbation for the landscapes. The nearest glacial activity is the Quaternary Lushan glacial which putatively happened locally in Lushan, north of Jiangxi province. However, the existence of the glacial activity itself is in dispute (Shi, 1982; Xie and Zhijiu, 1983). Furthermore, no reports cite evidence for its impact on the landscape in the study area. We therefore argue that it is reasonable to complete the modeling for the catena under the steady state assumption as articulated by Jin et al. (2010).

As discussed before, JLN-S4 is located on the hilltop and there is no evidence for other inputs of weathering products into it (other than atmospheric input which is ignored in the model). We also assume that the soil is creeping downslope along this catena, as assumed at Shale Hills (Jin et al., 2010). Following Jin et al. (2010), we assume the only input to the middle and bottom profiles are partially weathered materials from the upper slope. Lateral movement of material is assumed to occur from the hill top profile (JLN-S4, referred as HTP (hill top profile) in the model equations) to the hill middle profiles (JLN-S3 and JLN-S2), and then to the hill bottom profile (JLN-S1, referred as HBP (hill bottom profile) in the model equations). A hypothetical profile in the middle point of the slope is estimated by averaging the chemical composition and the denudation rate of JLN-S2 and JLN-S3, and is labeled as HMP (hill middle profile). HTP, HMP, and HBP profiles are each assumed to represent a box of material transport following Jin et al. (2010). The length of the box is 21 m (1/3 of the distance between HTP and HBP), and the depth of the box at every point is 120 cm. Using soil density and the thickness of each sampled interval (Tables 1 and 2), the values were weight-averaged to estimate the average bulk chemical composition for each site (Table 6).

Following the hillslope evolution model by Jin et al. (2010), we assume that a steady state exists such that the mass of soil produced per unit area per unit time (P) is equal to the mass that is transported out of a given box on the hillslope per unit area per unit time (D). The mass balance equations for this steady state can be written as follows for the ridgetop HTP for the immobile (i) and mobile (j) elements:

$$P = D = W + E \tag{4}$$

$$P^{HTP} C_{i,p} = E^{HTP} C_{i,HTP} \tag{5}$$

$$P^{HTP} C_{j,p} = E^{HTP} C_{j,HTP} + W_j^{HTP}. \tag{6}$$

P, D, W and E are the soil production rate, total denudation rate (physical + chemical), chemical weathering rate and erosion rate of the profile respectively (in g m^{-2} y^{-1}). $C_{i,HTP}$ and $C_{j,HTP}$ are the average chemical composition of the profile (oxide wt.%) for an immobile element (here we use Ti) or mobile element (j); $C_{i,p}$ and $C_{j,p}$ are the relevant concentrations in the bedrock (JLN-R3). The chemical composition data for each site and JLN-R3 are summarized in Table 6. Here D is set equal to the cosmogenic nuclide rate corrected by soil horizon average density for each site.

By rearranging Eqs. (4)–(6), the total chemical weathering rate W (including all elements, in units of g m^{-2} y^{-1}) for the HTP profile and for each element (W_j^{HTP}) can be calculated as shown below:

$$W^{HTP} = P^{HTP}(1 - C_{i,p}/C_{i,HTP}) \tag{7}$$

$$W_j^{HTP} = P^{HTP}(C_{j,p} - (C_{i,p}/C_{i,HTP})C_{j,HTP}). \tag{8}$$

We can also calculate the chemical depletion factor (CDF): CDF was defined by Riebe et al. (2003) to describe the contribution of chemical weathering relative to the total denudation flux. Noting our assumption that D = P, CDF for HTP profile (CDF^{HTP}) and individual element (CDF_j^{HTP}) can be calculated as:

$$CDF^{HTP} = W^{HTP}/P^{HTP} = W^{HTP}/D^{HTP} = 1 - C_{i,p}/C_{i,HTP} \tag{9}$$

$$CDF_j^{HTP} = 1 - (C_{j,HTP}C_{i,p})/(C_{j,p}C_{i,HTP}). \tag{10}$$

Table 6
Average soil chemistry at each site along the hillslope.

	SiO_2 (%)	TiO_2 (%)	P_2O_5 (%)	MnO (%)	Al_2O_3 (%)	CaO (%)	Na_2O (%)	K_2O (%)	TFe_2O_3 (%)	MgO (%)	Si/Al (molar)	Fe/Al (molar)	K/Al (molar)	Mg/Al (molar)
HTP	65.87	0.35	0.02	0.01	20.23	0.02	0.02	0.28	4.93	0.09	2.8	0.2	0.01	0.01
HMP	69.53	0.27	0.02	0.01	18.25	0.02	0.02	0.76	3.85	0.08	3.2	0.1	0.02	0.01
HBP	67.94	0.31	0.03	0.01	17.81	0.02	0.04	1.45	4.12	0.12	3.2	0.2	0.04	0.01
JLN-R3	73.58	0.20	0.04	0.07	13.25	0.95	3.19	5.15	2.37	0.18	4.7	0.1	0.21	0.02

The physical erosion rate E^{HTP} (in g m^{-2} y^{-1}) and the physical erosive output flux Q^{HTP} (in g m^{-1} y^{-1}) of the profile can be calculated with soil production rate, box length (21 m), and the profile and bedrock chemical composition by the following equations following Jin et al. (2010):

$$E^{HTP} = P^{HTP} C_{i,p} / C_{i,HTP} \quad (11)$$

$$Q^{HTP} = E^{HTP} L. \quad (12)$$

Like the hillslope evolution model from Jin et al. (2010), the middle and bottom hillslope profiles receive net physical erosion input. This input is defined as the difference between the material influx to the box and output.

So, the following equations can be written for HMP:

$$E^{HMP} = \left(Q^{HMP} - Q^{HTP}\right)/L \quad (13)$$

$$P^{HMP} = E^{HMP} + W^{HMP}. \quad (14)$$

Like Eqs. (7)–(12) for HTP, these equations can be rearranged to yield W^{HMP}, E^{HMP}, Q^{HMP}, W_j^{HMP} and CDF^{HMP} as follows:

$$W^{HMP} = P^{HMP}\left(1 - C_{i,p}/C_{i,HMP}\right) + E^{HTP}\left(1 - C_{i,HTP}/C_{i,HMP}\right) \quad (15)$$

$$E^{HMP} = P^{HMP}\left(C_{i,p}/C_{i,HMP}\right) - E^{HTP}\left(1 - C_{i,HTP}/C_{i,HMP}\right) \quad (16)$$

$$Q^{HMP} = \left(P^{HMP}\left(C_{i,p}/C_{i,HMP}\right) + E^{HTP}\left(C_{i,HTP}/C_{i,HMP}\right)\right)L \quad (17)$$

$$W_j^{HMP} = P^{HMP} C_{j,p}\left(1 - \left(C_{j,HMP} C_{i,p}\right)/\left(C_{j,p} C_{i,HMP}\right)\right) + E^{HTP} C_{j,HTP}\left(1 - \left(C_{j,HMP} C_{i,HTP}\right)/\left(C_{j,HTP} C_{i,HMP}\right)\right) \quad (18)$$

$$CDF^{HMP} = W^{HMP}/P^{HMP} = 1 - C_{i,p}/C_{i,HMP} + E^{HTP}/P^{HMP}\left(1 - C_{i,HTP}/C_{i,HMP}\right). \quad (19)$$

We can establish a similar set of equations for the bottom profile HBP, with material transported from HMP as its input.

The weathering output flux of each box F_j (in g m^{-1} y^{-1}) can be calculated with weathering rate W and box length (21 m) as follows:

$$F_j^{HTP} = W_j^{HTP} L \quad (20)$$

$$F_j^{HMP} = W_j^{HMP} L + F_j^{HTP} \quad (21)$$

$$F_j^{HBP} = W_j^{HBP} L + F_j^{HMP}. \quad (22)$$

Under the assumption of a time-independent weathering rate, we can solve the mass basis system of equations. We assume the denudation rate (D) in the mass balance equations equals the average bulk soil density corrected denudation rates inferred from cosmogenic nuclide concentration (^{26}Al, ^{10}Be) at each profile (Cui, 2014), the chemical composition for the catena positions equal the profile average values (Table 6), and the box lengths equal 21 m. Values of E, W, and CDF for top, middle and bottom sites are given in Table 7 and Fig. 10, as well as the chemical weathering rates and fluxes for individual element and their molar ratios.

The largest variations in model-calculated values along the hillslope (Fig. 10) are seen in E and P. In other words, the weathering rate W varies little across the catena according to this model. The physical erosion rate E for the middle slope is about 3–4 times higher than the top and bottom sites (Fig. 10a). This observation, derived from the equations because D was measured to be higher at these sites, is consistent with the higher curvature at the middle slope (HMP box in the model) (Fig. 1). Curvature affects both physical and chemical weathering (Lebedeva and Brantley, 2013). Effects of curvature on chemical weathering are discussed below for individual element.

Table 7
Mass-balance model results for the soil horizon of the studied hillslope.

	Hill top	Middle slope	Hill Bottom
P (g m^{-2} y^{-1})	26	55	24
W (g m^{-2} y^{-1})	11	11	14
E (g m^{-2} y^{-1})	15	44	10
CDF	0.4	0.2	0.6
Q = E * L (g m^{-1} y^{-1})	319	1241	1133
F = W * L (g m^{-1} y^{-1})	231	464	750
W_{si} (g m^{-2} y^{-1})	4.3	4.4	5.3
$F_{si} = W_{si} * L$ (g m^{-1} y^{-1})	91.1	183.0	293.9
W_P (g m^{-2} y^{-1})	0.0	0.0	0.0
$F_P = W_P * L$ (g m^{-1} y^{-1})	0.1	0.2	0.2
W_{Mn} (g m^{-2} y^{-1})	0.0	0.0	0.0
$F_{Mn} = W_{Mn} * L$ (g m^{-1} y^{-1})	0.3	0.8	1.0
W_{Al} (g m^{-2} y^{-1})	0.2	−0.2	0.8
$F_{Al} = W_{Al} * L$ (g m^{-1} y^{-1})	4.5	−0.3	16.8
W_{Ca} (g m^{-2} y^{-1})	0.2	0.4	0.2
$F_{Ca} = W_{Ca} * L$ (g m^{-1} y^{-1})	3.7	11.4	14.7
W_{Na} (g m^{-2} y^{-1})	0.6	1.3	0.6
$F_{Na} = W_{Na} * L$ (g m^{-1} y^{-1})	13.0	40.1	51.6
W_K (g m^{-2} y^{-1})	1.1	2.0	0.6
$F_K = W_K * L$ (g m^{-1} y^{-1})	22.8	65.1	78.5
W_{Fe} (g m^{-2} y^{-1})	−0.1	−0.2	0.0
$F_{Fe} = W_{Fe} * L$ (g m^{-1} y^{-1})	−1.9	−5.2	−4.7
W_{Mg} (g m^{-2} y^{-1})	0.0	0.0	0.0
$F_{Mg} = W_{Mg} * L$ (g m^{-1} y^{-1})	0.4	1.2	1.4
F_{Si}/F_{Al} (molar)[a]	20		17
F_{Ca}/F_{Al} (molar)	1		1
F_{Na}/F_{Al} (molar)	3		4
F_K/F_{Al} (molar)	4		3
F_{Fe}/F_{Al} (molar)	0		0
F_{Mg}/F_{Al} (molar)	0		0

[a] Molar ratio of chemical weathering fluxes F_j.

The CDF calculated from the equations above vary from 0.2 to 0.6, i.e. 20 to 60% of the material lost to denudation was lost by chemical weathering (Table 7). In contrast, CDF values calculated from the original definition of CDF (Riebe et al., 2003) for each site vary between 0.3 and 0.4. Given some of the model assumptions for the calculation from Eq. (19), this level of discrepancy is not surprising. These calculations lead to the inference that somewhere between 1/5 to 2/3 of the material along this ridgeline has been lost by chemical weathering. Furthermore, Figs. 5 and 6 show that the percent loss of a given element can vary even larger: e.g., fractional loss of K by solubilization is highest at the hilltop where it approaches 100%, and decreases toward the road outcrop where it is closer to 80%.

Such variations in primary mineral content in topsoil down a hillslope have been simulated in weathering models based on geochemical processes, i.e., more primary mineral can be retained at the land surface at the bottom of a hillslope (here, K feldspar) compared to the top of the hillslope (see Fig. 4) when denudation of the entire hillslope occurs in a mixed regime. In such a mixed regime, chemical weathering is rate-limiting at the bottom of the hillslope but physical erosive transport is limiting at the top (Lebedeva and Brantley, 2013).

SiO_2 accounts for about 84% of the chemical weathering outflux from the soil horizons along the ridgeline hillslope. Molar ratios of chemical weathering fluxes of Si and Al (F_{Si}/F_{Al}) for the top and bottom sites are 20 and 17 respectively, much higher than the average bulk chemical composition of the top site (2.8) and bottom site (3.2) (Tables 6 and 7). As discussed in Section 4.1, quartz dissolution and kaolinite transformation to gibbsite dominate the weathering reactions in the soil horizon (Fig. 8), releasing Si. The molar ratios with respect to Al for the calculated chemical weathering fluxes for the base cations (K, Na, Ca and Mg) for top and bottom sites are also similar, and again larger than the ratios in the soils. This result differs from the similarity observed between weathering fluxes and soil chemistry in the Susquehannna/Shale Hills study (Jin et al., 2010). One conclusion from the shale study

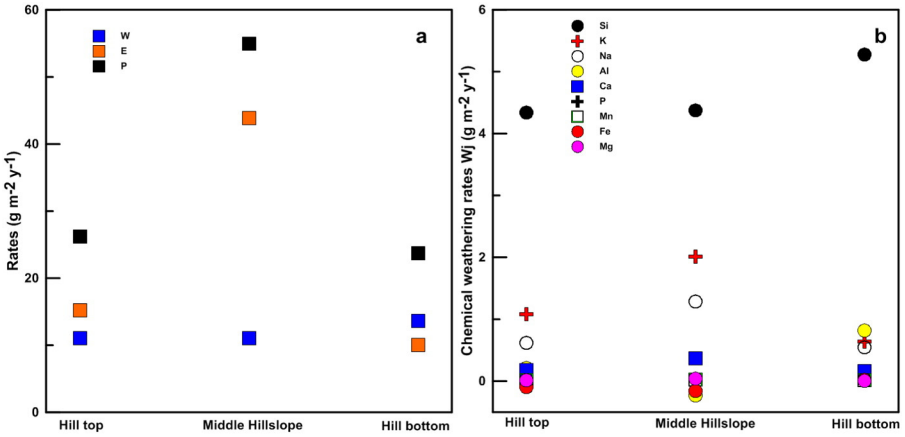

Fig. 10. Model-calculated net chemical weathering rates (W), physical erosion rates (E) and soil production rates (P) (a) and chemical weathering rates for individual element (b) as a function of topographic location along the hillslope, as described in text.

was that much of the "chemical weathering" of the shale was due to subsurface fine particle transport rather than solute transport; therefore, element release ratios were similar to shale soil ratios. In contrast, for this granite, quartz, K feldspar, and kaolinite are the predominant minerals weathering in the topsoil and the ratios of W calculated for individual elements for the soil differ from element ratios in the original granite. In other words, as expected, fine particle transport in the subsurface is not as important in the granite as it is in the shale studied by Jin et al. (2010).

Fig. 10 also shows that the Al chemical weathering outflux at the bottom site (16.8 g m^{-1} y^{-1}) is about four times that of the top site (4.5 g m^{-1} y^{-1}). Kaolinite and gibbsite are the dominant minerals containing Al at the hilltop, and both minerals are relatively stable in circumneutral-pH waters lacking high concentrations of organic ligands. At pH less than 5, Al becomes mobile and is released from aluminosilicates (Jackson, 1963). The rate of Al loss is presumably higher from the bottom site because of the high surface area provided by the fine particles of K-feldspar present in the bottom site (Table 7 and Fig. 10b) and because of the low pH in the soil horizon of JLN-S1 (Fig. 2). An explanation for the slight accumulation of Al at middle slope (Table 7) could be that the Al released from the upper sites by chemical weathering is carried downslope and precipitated in the middle slope sites where curvature changes (Fig. 1), perhaps due to pH increases (see Section 4.3). In contrast, Fe shows net accumulation over the whole catena (F_{Fe}: −1.9, −5.2, −4.7 g m^{-1} y^{-1} from top to bottom site). This accumulation might be affected by bio-pumping as discussed in Section 4.1.

In contrast to the hillslope evolution research of Susquehannna/Shale Hills (Jin et al., 2010) and Frog's Hollow in New South Wales (Yoo et al., 2007), the overall weathering rate in this study is higher at the bottom site. The hillslope valley site described by Jin et al. (2010) exhibits the lowest calculated weathering rate of the shale transect. Jin et al. (2010) attributed slow weathering near the valley at least partly to increases in dissolved solutes along the flowpath downslope, pointing out that some elements were even precipitating as secondary minerals in the valley site. In contrast, the bottom profile of our granite site may receive downslope-transported organic material and primary silicate particles that enhance weathering rates. An even bigger factor may be that the Shale Hills profile is concave near valley bottom whereas the land surface curvature of the bottom site in our catena is near-linear. Furthermore, here the catena is located along the nose of a ridgeline aligned parallel with the stream (Fig. 1), which is in contrast to the planar hillslope above a first-order channel described by Jin et al. (2010). All of these characteristics may affect chemical weathering in the downslope site of the granite.

We can also look at individual element weathering rates along the catena. K and Na chemical weathering rates are highest in the high-curvature middle of the transect compared to above and below (Table 7 and Fig. 10). The chemical release rates for K and Na were also observed to be largest in the middle site of Frog's Hollow (Yoo et al., 2007) (Fig. 10). In contrast, Si and Al chemical release rates are approximately the same at the top and mid-slope but increase at the bottom site of our granite catena (Table 7 and Fig. 10). Apparently, dissolution of primary mineral (feldspar) is fastest in the mid-slope high-curvature site but dissolution of secondary mineral (kaolinite) is fastest in the bottom site. One explanation could be that as kaolinite dissolves toward the bottom of the hillslope – perhaps due to a higher organic ligand content in porewaters – weathering solutions increase in Si concentration and move closer to equilibrium with K feldspar, slowing the rate of dissolution of that mineral in the downslope position. In addition, it is possible that weathering of primary minerals is tightly coupled with soil production rate (which is highest mid-slope) whereas weathering of secondary minerals is not. Such mechanisms cannot be entirely understood unless the soil solution chemistries and hydrologic flow paths along the slope are measured.

5. Conclusions

The studied profiles present a representative example of granite weathering and pedogenesis in a sub-tropical climate. A weathering sequence of granite is delineated by mineralogy and major element variation. Apatite, biotite, hornblende and plagioclase are dissolved in the initial weathering stage. Nearly 100% Ca and Na loss happens at depth in this stage; Mg, Fe and P also reach their maximum extent of depletion at the end of this stage. The K-feldspar reaction front begins after complete depletion in plagioclase, resulting in about 80% loss of K at the land surface at the bottom of the ridgeline and almost 100% loss at the top. Quartz dissolution begins after much of the K-feldspar has been depleted, resulting in about 60% Si release at the land surface of the ridgeline. As the dominant clay mineral, kaolinite is the weathering product of feldspar during the whole weathering process. Kaolinite transforms to gibbsite which is the terminal weathering product as weathering proceeds.

In the upper 100 cm, many effects of biological activity are observed, as well as the effects of physical erosion and chemical weathering. This topsoil has low pH, and is characterized by intensive fragmentation and dissolution of quartz, a high clay mineral and high TOC content.

Lateral movement of weathering products – both primary mineral particles and organic matter – down the ridgeline is inferred. A simple mass balance calculation of chemical and physical weathering based on the topsoil chemistry at four sites along the ridgeline shows that chemical weathering rates are accelerated at the bottom site where high organic content was noted. The middle site was calculated to have the highest physical erosion rates, perhaps due to the higher curvature at middle slope.

The granite weathering and pedogenic processes documented here show that reaction fronts for minerals are separated over meters in depth: ferrous silicate minerals react first, followed by plagioclase, then K-feldspar, and finally, kaolinite and quartz. Landscape position is a critical factor in controlling the extent of silicate weathering in granite due to coupling of physical erosion and chemical weathering. Further studies on elemental and isotopic geochemical indices are needed to explore different granite weathering stages and their significance on basin-scale chemical weathering.

Acknowledgments

This work was financially supported by the National Basic Research Program of China ("973 Program", Grant No. 2013CB956401), the "Strategic Priority Research Program" of the Chinese Academy of Sciences (Grant No. XDB15010405), National Natural Science Foundation of China (Grant No. 41130536 and 41402323) and the International Postdoctoral Exchange Fellowship Program (Grant No. 20140045). Susan L. Brantley and Wenjing Liu acknowledge the support from grant DE-FG02-OSER15675 from the U.S. Department of Energy Office of Basic Energy Sciences for work on chemical weathering. The authors are grateful to Shanke Liu in Institute of Geology and Geophysics, Chinese Academy of Sciences, and Dr. Scott Hynek in the Earth and Environmental Systems Institute, The Pennsylvania State University for their communication. The paper benefited much from insightful comments and suggestions from the handling editor and an anonymous reviewer.

Appendix A. The best analyzing range and accuracy of the Axios XRF in this study

Compound	Best analyzing range (%)	Accuracy (%)
SiO_2	15.0–95.0	±0.20
TiO_2	0.01–7.50	±0.005
Al_2O_3	0.20–25.0	±0.10
TFe_2O_3	0.20–25.0	±0.05
MnO	0.01–0.35	±0.005
MgO	0.20–40.0	±0.03
CaO	0.10–35.0	±0.03
Na_2O	0.10–7.50	±0.03
K_2O	0.05–7.50	±0.02
P_2O_5	0.01–1.00	±0.005
FeO_T	0.20–20.0	±0.10

Appendix B. Standard of deviation calculation for the major elements of the four bedrock samples

Sample no.	SiO_2 (%)	TiO_2 (%)	P_2O_5 (%)	MnO (%)	Al_2O_3 (%)	CaO (%)	Na_2O (%)	K_2O (%)	FeO_T (%)	MgO (%)	LOI (%)
JLN-R1	74.10	0.20	0.03	0.06	12.89	0.87	3.10	5.24	2.43	0.18	0.60
JLN-R2	73.00	0.22	0.04	0.07	13.07	1.02	3.34	5.10	2.76	0.21	0.48
JLN-R3	73.58	0.20	0.04	0.07	13.25	0.95	3.19	5.15	2.37	0.18	0.42
JLN-R4	74.64	0.24	0.05	0.05	12.68	0.48	3.18	4.68	2.97	0.21	0.68
Average	73.83	0.22	0.04	0.06	12.97	0.83	3.20	5.04	2.63	0.19	0.54
Standard of deviation	0.70	0.02	0.01	0.01	0.24	0.24	0.10	0.25	0.28	0.02	0.12

References

Babechuk, M.G., Widdowson, M., Kamber, B.S., 2014. Quantifying chemical weathering intensity and trace element release from two contrasting basalt profiles, Deccan Traps, India. Chem. Geol. 363 (0), 56–75.
Bengtsson, H., Stevens, R.L., 1998. Source and grain-size influences upon the clay mineral distribution in the Skagerrak and northern Kattegat. Clay Miner. 33 (1), 3–13.
Bern, C.R., Chadwick, O.A., Hartshorn, A.S., Khomo, L.M., Chorover, J., 2011. A mass-balance model to separate and quantify colloidal and solute redistributions in soil. Chem. Geol. 282 (3–4), 113–119.
Berner, R.A., Lasaga, A.C., Garrels, R.M., 1983. The carbonate–silicate geochemical cycle and its effect on atmospheric carbon-dioxide over the past 100 million years. Am. J. Sci. 283 (7), 641–683.
Bloom, Paul R., Skyllberg, Ulf, 2011. Soil pH and pH buffering. In: Huang, P.M., Li, Y., Sumner, M.E. (Eds.), Handbook of Soil Sciences. Properties and Processes. CRC Press, Boca Raton, FL, p. 1442 (2011).
Blum, J.D., Erel, Y., 1997. Rb–Sr isotope systematics of a granitic soil chronosequence: the importance of biotite weathering. Geochim. Cosmochim. Acta 61 (15), 3193–3204.
Bouchez, J., Gaillardet, J., 2014. How accurate are rivers as gauges of chemical denudation of the Earth surface? Geology 42, 171–174.
Brantley, S.L., Lebedeva, M., 2011. Learning to read the chemistry of regolith to understand the Critical Zone. Annu. Rev. Earth Planet. Sci. 39, 387–416.
Brantley, S.L., Lebedeva, M., Bazilevskaya, E., 2014. 6.15 — relating weathering fronts for acid neutralization and oxidation to p_{CO_2} and pO2. In: Turekian, H.D.H.K. (Ed.), Treatise on Geochemistry, second ed. Elsevier, Oxford, pp. 327–352.
Braun, J.J., Descloitres, M., Riotte, J., et al., 2009. Regolith mass balance inferred from combined mineralogical, geochemical and geophysical studies: Mule Hole gneissic watershed, South India. Geochim. Cosmochim. Acta 73 (4), 935–961.
Brimhall, G.H., Dietrich, W.E., 1987. Constitutive mass balance relations between chemical composition, volume, density, porosity, and strain in metasomatic hydrochemical systems: results on weathering and pedogenesis. Geochim. Cosmochim. Acta 51 (3), 567–587.
Burkins, D.L., Blum, J.D., Brown, K., et al., 1999. Chemistry and mineralogy of a granitic, glacial soil chronosequence, Sierra Nevada Mountains, California. Chem. Geol. 162 (1), 1–14.
Buss, H.L., Sak, P.B., Webb, S.M., Brantley, S.L., 2008. Weathering of the Rio Blanco quartz diorite, Luquillo Mountains, Puerto Rico: coupling oxidation, dissolution, and fracturing. Geochim. Cosmochim. Acta 72 (18), 4488–4507.
Ceryan, S., Zorlu, K., Gokceoglu, C., Temel, A., 2008. The use of cation packing index for characterizing the weathering degree of granitic rocks. Eng. Geol. 98 (1–2), 60–74.
Chen, P.R., Zhou, X.M., Zhang, W.L., et al., 2004. Petrogenesis and implication of early Yanshanian syenite–granite complex in Eastern Nanling Mountain Area. Sci. China Ser. D Earth Sci. 34 (6), 493–503 (in Chinese).
Chesworth, W., 1992. Weathering systems. In: Martini, I.P., Chesworth, W. (Eds.), Weathering, Soil and PaleosoilsDevelopments in Earth Surface Processes 2. Elsevier, Amsterdam, pp. 19–40.
Cui, Lifeng, 2014. The Denudation Rates of Granite Region in Eastern China: Results of Cosmogenic Nuclides ^{10}Be and ^{26}Al (Ph.D. thesis) Institute of Geochemistry, Chinese Academy of Sciences, pp. 1–96 (in Chinese with English abstract).
Dessert, C., Dupré, B., Gaillardet, J., et al., 2003. Basalt weathering laws and the impact of basalt weathering on the global carbon cycle. Chem. Geol. 202 (3–4), 257–273.
Driese, S.G., 2004. Pedogenic translocation of Fe in modern and ancient Vertisols and implications for interpretations of the Hekpoort paleosol (2.25 Ga). J. Geol. 112 (5), 543–560.
Dupré, B., et al., 2003. Rivers, chemical weathering and Earth's climate. Compt. Rendus Geosci. 335 (16), 1141–1160.
Duzgoren-Aydin, N.S., Aydin, A., 2009. Distribution of rare earth elements and oxyhydroxide phases within a weathered felsic igneous profile in Hong Kong. J. Asian Earth Sci. 34 (1), 1–9.
Fan, C.F., Chen, P.R., 2000. Nd and Sr isotopic compositions of Pitou granitoid in South Jiangxi Province. Geol. Prospect. Symp. 15 (3), 282–287 (in Chinese with English Abstract).
Fimmen, R., Richter Jr., D., Vasudevan, D., Williams, M., West, L., 2008. Rhizogenic Fe–C redox cycling: a hypothetical biogeochemical mechanism that drives crustal weathering in upland soils. Biogeochemistry 87 (2), 127–141.
Fujii, M., Imaoka, A., Yoshimura, C., Waite, T.D., 2014. Effects of molecular composition of natural organic matter on ferric iron complexation at circumneutral pH. Environ. Sci. Technol. 48 (8), 4414–4424.
Gaillardet, J., Dupré, B., Louvat, P., et al., 1999. Global silicate weathering and CO_2 consumption rates deduced from the chemistry of large rivers. Chem. Geol. 159 (1–4), 3–30.
Goddéris, Y., Donnadieu, Y., Tombozafy, M., Dessert, C., 2008. Shield effect on continental weathering: implication for climatic evolution of the Earth at the geological timescale. Geoderma 145 (3–4), 439–448.
Goldich, S.S., 1938. A study in rock weathering. J. Geol. 46, 17–58.
Green, E.G., Dietrich, W.E., Banfield, J.F., 2006. Quantification of chemical weathering rates across an actively eroding hillslope. Earth Planet. Sci. Lett. 242 (1–2), 155–169.
Hassellöv, M., et al., 2001. Particle size distributions of clay-rich sediments and pure clay minerals: a comparison of grain size analysis with sedimentation field-flow fractionation. Aquat. Geochem. 7 (2), 155–171.
Holland, H.D., Zbinden, E.A., 1988. Paleosols and the Evolution of the Atmosphere: Part I. In: Lerman, A., Meybeck, M. (Eds.), Physical and Chemical Weathering in Geochemical Cycles 251. Springer, Netherlands, pp. 61–82.
Hurowitz, J.A., et al., 2006. In situ and experimental evidence for acidic weathering of rocks and soils on Mars. J. Geophys. Res. Planets 111 (E2), E02S19.
Jackson, M.L., 1963. Aluminum bonding in soils: a unifying principle in soil science. Soil Sci. Soc. Am. Proc. 27, 1–10.
Jeong, G.Y., Bin Kim, H., 2003. Mineralogy, chemistry, and formation of oxidized biotite in the weathering profile of granitic rocks. Am. Mineral. 88 (2–3), 352–364.
Jin, L., Brantley, S.L., 2011. Soil chemistry and shale weathering on a hillslope influenced by convergent hydrologic flow regime at the Susquehanna/Shale Hills Critical Zone Observatory. Appl. Geochem. 26 (Supplement(0)), S51–S56.
Jin, L., et al., 2010. Mineral weathering and elemental transport during hillslope evolution at the Susquehanna/Shale Hills Critical Zone Observatory. Geochim. Cosmochim. Acta 74 (13), 3669–3691.

Kamei, A., Fukushi, K., Takagi, T., et al., 2012. Chemical overprinting of magmatism by weathering: a practical method for evaluating the degree of chemical weathering of granitoids. Appl. Geochem. 27 (3), 796–805.
Khomo, L., Bern, C.R., Hartshorn, A.S., Rogers, K.H., Chadwick, O.A., 2013. Chemical transfers along slowly eroding catenas developed on granitic cratons in southern Africa. Geoderma 202–203, 192–202.
Kirschbaum, A., Martínez, E., Pettinari, G., et al., 2005. Weathering profiles in granites, Sierra Norte (Córdoba, Argentina). J. S. Am. Earth Sci. 19 (4), 479–493.
Land, M., Ohlander, B., 2000. Chemical weathering rates, erosion rates and mobility of major and trace elements in a boreal granitic till. Aquat. Geochem. 6 (4), 435–460.
Law, K.R., Nesbitt, H.W., Longstaffe, F.J., 1991. Weathering of granitic tills and the genesis of a podzol. Am. J. Sci. 291 (10), 940–976.
Lebedeva, M.I., Brantley, S.L., 2013. Exploring geochemical controls on weathering and erosion of convex hillslopes: beyond the empirical regolith production function. Earth Surf. Process. Landf. 38 (15), 1793–1807.
Li, X.H., Li, W.X., Li, Z.X., 2007. Rethinking of petrogenesis and tectonic implication of early Yanshanian granite in Nanling Mountain area. Chin. Sci. Bull. 52 (9), 981–991 (in Chinese).
Liu, Wenjing, 2013. Element, Strontium and Lithium Isotope Geochemical Features and Their Implications for Weathering Processes of Granite in Longnan, Jiangxi Province, South China (Ph.D. thesis) Institute of Geochemistry, Chinese Academy of Sciences, pp. 1–119 (in Chinese with English abstract).
Ma, J., Wei, G., Xu, Y., Long, W., Sun, W., 2007. Mobilization and re-distribution of major and trace elements during extreme weathering of basalt in Hainan Island, South China. Geochim. Cosmochim. Acta 71 (13), 3223–3237.
Ma, J., Wei, G., Xu, Y., Long, W., 2010a. Variations of Sr–Nd–Hf isotopic systematics in basalt during intensive weathering. Chem. Geol. 269 (3–4), 376–385.
Ma, L., et al., 2010b. Regolith production rates calculated with uranium-series isotopes at Susquehanna/Shale Hills Critical Zone Observatory. Earth Planet. Sci. Lett. 297 (1–2), 211–225.
Ma, L., Jin, L., Brantley, S.L., 2011. How mineralogy and slope aspect affect REE release and fractionation during shale weathering in the Susquehanna/Shale Hills Critical Zone Observatory. Chem. Geol. 290 (1–2), 31–49.
Manikyamba, C., Kerrich, R., Gonzáez-Avarez, I., Mathur, R., Khanna, T.C., 2008. Geochemistry of Paleoproterozoic black shales from the Intracontinental Cuddapah basin, India: implications for provenance, tectonic setting, and weathering intensity. Precambrian Res. 162 (3–4), 424–440.
McKnight, D.M., Scott, D.T., Lovley, D.R., 2001. Photochemical and microbial processes influencing iron–humic interactions in stream and lake sediments. In: Clapp, C.E., Hayes, M.H.B., Senesi, N., Bloom, P.R., Jardine, P.M. (Eds.), Humic Substances and Chemical Contaminants. Soil Science Society of America, Madison, WI.
McLennan, S.M., 2001. Relationships between the trace element composition of sedimentary rocks and upper continental crust. Geochem. Geophys. Geosyst. 2. http://dx.doi.org/10.1029/2000GC000109.
Middelburg, J.J., van der Weijden, C.H., Woittiez, J.R.W., 1988. Chemical processes affecting the mobility of major, minor and trace elements during weathering of granitic rocks. Chem. Geol. 68 (3–4), 253–273.
Millero, F.J., Yao, W., Aicher, J., 1995. The speciation of Fe(II) and Fe(III) in natural waters. Mar. Chem. 50 (1–4), 21–39.
Minařík, L., Žigová, A., Bendl, J., Skřivan, P., Šťastný, M., 1998. The behaviour of rare-earth elements and Y during the rock weathering and soil formation in the Říčany granite massif, Central Bohemia. Sci. Total Environ. 215 (1–2), 101–111.
Mongelli, G., 1993. REE and other trace elements in a granitic weathering profile from "Serre", southern Italy. Chem. Geol. 103 (1–4), 17–25.
Navarre-Sitchler, A., Brantley, S.L., Rother, G., 2015. How porosity increases during incipient weathering of crystalline silicate rocks. Rev. Mineral. Geochem. 80 (1), 331–354.
Négrel, P., 2006. Water–granite interaction: clues from strontium, neodymium and rare earth elements in soil and waters. Appl. Geochem. 21 (8), 1432–1454.
Nesbitt, H.W., 1979. Mobility and fractionation of rare earth elements during weathering of a granodiorite. Nature 279 (5710), 206–210.
Nesbitt, H.W., Markovics, G., Price, R.C., 1980. Chemical processes affecting alkalis and alkaline earths during continental weathering. Geochim. Cosmochim. Acta 44 (11), 1659–1666.
Nesbitt, H.W., Young, G.M., 1982. Early Proterozoic climates and plate motions inferred from major element chemistry of lutites. Nature 299 (5885), 715–717.
Nesbitt, H.W., Young, G.M., 1984. Prediction of some weathering trends of plutonic and volcanic rocks based on thermodynamic and kinetic considerations. Geochim. Cosmochim. Acta 48 (7), 1523–1534.
Oliva, P., Viers, J., Dupré, B., 2003. Chemical weathering in granitic environments. Chem. Geol. 202 (3–4), 225–256.
Pansu, M., Gautheyrou, J., 2007. Handbook of Soil Analysis: Mineralogical, Organic and Inorganic Methods. Springer Science & Business Media, pp. 732–735.
Pavich, M.J., Leo, G.W., Obermeier, S.F., Estabrook, J.R., 1989. Investigations of the Characteristics, Origin, and Residence Time of the Upland Residual Mantle of the Piedmont of Fairfax County, Virginia. United States Government Printing Office, Washington, p. 5.
Pehlivanoglou, K.G., Trontsios, G., Tsirambides, A., 2004. Grain size distribution, clay mineralogy and chemistry of bottom sediments from the outer Thermaikos Gulf, Aegean Sea, Greece. Mediterr. Mar. Sci. 5 (1), 43–53.
Pett-Ridge, J.C., Derry, L.A., Kurtz, A.C., 2009. Sr isotopes as a tracer of weathering processes and dust inputs in a tropical granitoid watershed, Luquillo Mountains, Puerto Rico. Geochim. Cosmochim. Acta 73 (1), 25–43.
Prudêncio, M.I., Braga, M.A.S., Gouveia, M.A., 1993. REE mobilization, fractionation and precipitation during weathering of basalts. Chem. Geol. 107 (3–4), 251–254.
Riebe, C.S., Kirchner, J.W., Finkel, R.C., 2003. Long-term rates of chemical weathering and physical erosion from cosmogenic nuclides and geochemical mass balance. Geochim. Cosmochim. Acta 67, 4411–4427.
Robert, M., Tessier, D., 1992. Incipient weathering: some new concept on weathering, clay formation and organization. In: Martini, I.P., Chesworth, W. (Eds.), Weathering, Soil and Paleosoils, Developments in Earth Surface Processes 2. Elsevier, Amsterdam, pp. 71–105.
Rudnick, R.L., Tomascak, P.B., Njo, H.B., Gardner, L.R., 2004. Extreme lithium isotopic fractionation during continental weathering revealed in saprolites from South Carolina. Chem. Geol. 212 (1–2), 45–57.
Rye, R., Holland, H.D., 2000. Geology and geochemistry of paleosols developed on the Hekpoort basalt, Pretoria Group, South Africa. Am. J. Sci. 300 (2), 85–141.
Sequeira Braga, M.A., Paquet, H., Begonha, A., 2002. Weathering of granites in a temperate climate (NW Portugal): granitic saprolites and arenization. Catena 49, 41–56.
Shalkowski, A., Kodama, Y., Nakano, S., 2009. The assessment of weathering stages in granites using an EC/pH meter. Geomorphology 105 (3–4), 253–260.
Shi, Yafeng, 1982. Is there really quaternary glaciation on Lushan? Glacier and Tundra 4 (1), 64–69 (in Chinese with English Abstract).
Taylor, S.R., McLennan, S.M., 1985. The Continental Crust: Its Composition and Evolution. Blackwell, Oxford (312 pp.).
Turner, B.F., Stallard, R.F., Brantley, S.L., 2003. Investigation of in situ weathering of quartz diorite bedrock in the Rio Icacos basin, Luquillo Experimental Forest, Puerto Rico. Chem. Geol. 202 (3–4), 313–341.
Tuttle, M.L.W., Breit, G.N., 2009. Weathering of the New Albany Shale, Kentucky, USA: I. Weathering zones defined by mineralogy and major-element composition. Appl. Geochem. 24 (8), 1549–1564.
Volk, T., 1987. Feedbacks between weathering and atmospheric CO_2 over the last 100 million years. Am. J. Sci. 287 (8), 763–779.
Walker James, C.G., Hays, P.B., Kasting, J.F., 1981. A negative feedback mechanism for the long-term stabilization of earth's surface temperature[J]. J. Geophys. Res. 86 (C10), 9776–9782.
White, A.F., Bullen, T.D., Vivit, D.V., Schulz, M.S., Clow, D.W., 1999. The role of disseminated calcite in the chemical weathering of granitoid rocks. Geochim. Cosmochim. Acta 63 (13–14), 1939–1953.
White, A.F., Thomas, D.B., Marjorie, S.S., et al., 2001. Differential rates of feldspar weathering in granitic regoliths. Geochim. Cosmochim. Acta 65 (6), 847–869.
White, A.F., et al., 2008. Chemical weathering of a marine terrace chronosequence, Santa Cruz, California I: interpreting rates and controls based on soil concentration–depth profiles. Geochim. Cosmochim. Acta 72 (1), 36–68.
Xie, Youyu, Zhijiu, Cui, 1983. On nonglacial genesis of "Glaciated relics" of Lushan. 38 (3), 298–309 (in Chinese with English Abstract).
Yoo, K., Amundson, R., Heimsath, A.M., Dietrich, W.E., Brimhall, G.H., 2007. Integration of geochemical mass balance with sediment transport to calculate rates of soil chemical weathering and transport on hillslopes. J. Geophys. Res. Earth Surf. 112 (F2), 2003–2012.
Zhang, Z.-J., Liu, C.-Q., Zhao, Z.-Q., et al., 2015. Behavior of redox-sensitive elements during weathering of granite in subtropical area using X-ray absorption fine structure spectroscopy. J. Asian Earth Sci. 105, 418–429.